

Neural Sinkhorn Gradient Flow

Huminhao Zhu¹, Fangyikang Wang¹, Chao Zhang¹, Hanbin Zhao¹ and Hui Qian¹

¹College of Computer Science and Technology, Zhejiang University

{zhuhuminhao, wangfangyikang, zczju, zhaohanbin, qianhui}@zju.edu.cn

Abstract

Wasserstein Gradient Flows (WGF) with respect to specific functionals have been widely used in the machine learning literature. Recently, neural networks have been adopted to approximate certain intractable parts of the underlying Wasserstein gradient flow and result in efficient inference procedures. In this paper, we introduce the Neural Sinkhorn Gradient Flow (NSGF) model, which parametrizes the time-varying velocity field of the Wasserstein gradient flow w.r.t. the Sinkhorn divergence to the target distribution starting a given source distribution. We utilize the velocity field matching training scheme in NSGF, which only requires samples from the source and target distribution to compute an empirical velocity field approximation. Our theoretical analyses show that as the sample size increases to infinity, the mean-field limit of the empirical approximation converges to the true underlying velocity field. To further enhance model efficiency on high-dimensional tasks, a two-phase NSGF++ model is devised, which first follows the Sinkhorn flow to approach the image manifold quickly (≤ 5 NFEs) and then refines the samples along a simple straight flow. Numerical experiments with synthetic and real-world benchmark datasets support our theoretical results and demonstrate the effectiveness of the proposed methods.

1 Introduction

The Wasserstein Gradient Flow (WGF) with respect to certain specific functional objective \mathcal{F} (denoted as \mathcal{F} Wasserstein gradient flow) is a powerful tool for solving optimization problems over the Wasserstein probability space. Since the seminal work of [Jordan *et al.*, 1998] which shows that the Fokker-Plank equation is the Wasserstein gradient flow with respect to the free energy, Wasserstein gradient flow w.r.t. different functionals have been widely used in various machine learning tasks such as Bayesian inference [Zhang *et al.*, 2021a], reinforcement learning [Zhang *et al.*, 2021b], and mean-field games [Zhang and Katsoulakis, 2023].

One recent trend in the Wasserstein gradient flow literature is to develop efficient generative modeling methods

[Gao *et al.*, 2019; Gao *et al.*, 2022; Ansari *et al.*, 2021; Mokrov *et al.*, 2021; Alvarez-Melis *et al.*, 2022; Bunne *et al.*, 2022; Fan *et al.*, 2022]. In general, these methods mimic the Wasserstein gradient flow with respect to a specific distribution metric, driving a source distribution towards a target distribution. Neural networks are typically employed to approximate the computationally challenging components of the underlying Wasserstein gradient flow such as the time-dependent transport maps. During the training process of these methods, it is common to require samples from the target distribution. After the training process, an inference procedure is often employed to generate new samples from the target distribution. This procedure involves iteratively transporting samples from the source distribution with the assistance of the trained neural network. Based on the chosen metric, these methods can be categorized into two main types.

Divergences Between Distributions With Exact Same Supports. The first class of widely used metrics is the f-divergence, such as the Kullback-Leibler divergence and the Jensen-Shannon divergence. These divergences are defined based on the density ratio between two distributions and are only well-defined when dealing with distributions that have exactly the same support. Within the scope of f-divergence Wasserstein gradient flow generative models, neural networks are commonly utilized to formulate density-ratio estimators, as demonstrated by [Gao *et al.*, 2019; Ansari *et al.*, 2021] and [Heng *et al.*, 2022]. However, as one can only access finite samples from target distributions in the training process, the support shift between the sample collections from the compared distributions may cause significant approximation error in the density-ratio estimators [Choi *et al.*, 2022]. An alternative approach, proposed by [Fan *et al.*, 2022], circumvents these limitations by employing a dual variational formulation of the f-divergence. In this framework, two networks are employed to approximate the optimal variational function and the transport maps. These two components are optimized alternately. It's imperative to highlight that the non-convex and non-concave characteristics of their min-max objective can render the training inherently unstable [Hsieh *et al.*, 2021].

Divergences Between Distributions With Possible Different Supports. Another type of generative Wasserstein gradient flow model employs divergences that are well-defined for distributions with possible different supports. This includes free energy functionals [Mokrov *et al.*, 2021;

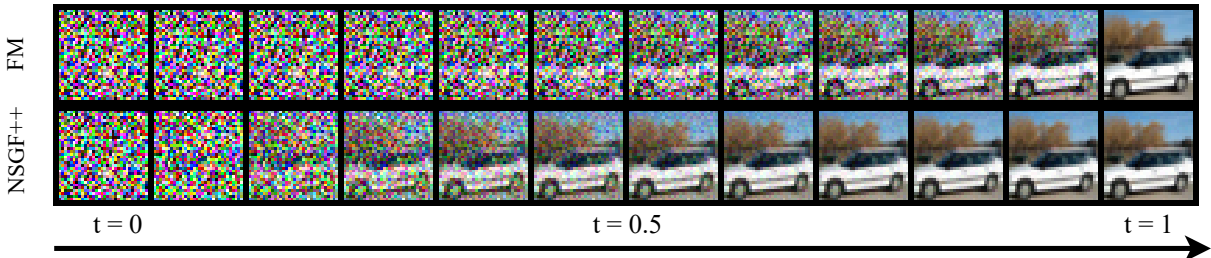


Figure 1: Trajectories comparison between the Flow matching and the NSGF++ model in CIFAR-10 task. we can see NSGF++ model quickly recovers the target structure and progressively optimizes the details in subsequent steps

Bunne *et al.*, 2022], the kernel-based metrics such as the Maximum-Mean/Sobolev Discrepancy [Mroueh *et al.*, 2019; Mroueh and Rigotti, 2020] and sliced-Wasserstein distance [Liutkus *et al.*, 2019; Du *et al.*, 2023]. As these divergences can be efficiently approximated with samples, neural networks are typically used to directly model the transport maps used in the inference procedure. In Wasserstein gradient flow methods, input convex neural networks (ICNNs, [Amos *et al.*, 2017]) are commonly used to approximate the transport map. However, recently, several works [Korotin *et al.*, 2021] discuss the poor expressiveness of ICNNs architecture and show that it would result in poor performance in high-dimension applications. Besides, the Maximum-Mean/Sobolev discrepancy Wasserstein gradient flow models are usually hard to train and are easy to trapped in poor local optima in practice [Arbel *et al.*, 2019], since the kernel-based divergences are highly sensitive to the parameters of the kernel function [Li *et al.*, 2017; Wang *et al.*, 2018]. [Liutkus *et al.*, 2019; Du *et al.*, 2023] consider sliced-Wasserstein WGF to build nonparametric generative Models which do not achieve high generation quality, it is an interesting work on how to combine sliced-Wasserstein WGF and neural network methods.

Contribution. In this paper, we investigate the Wasserstein gradient flow with respect to the Sinkhorn divergence, which is categorized under the second type of divergence and does not necessitate any kernel functions. We introduce the *Neural Sinkhorn Gradient Flow (NSGF)* model, which parametrizes the time-varying velocity field of the Sinkhorn Wasserstein gradient flow from a specified source distribution. The NSGF employs a velocity field matching scheme that demands only samples from the target distribution to calculate empirical velocity field approximations. Our theoretical analyses show that as the sample size approaches infinity, the mean-field limit of the empirical approximation converges to the true velocity field of the Sinkhorn Wasserstein gradient flow. Given distinct source and target data samples, our NSGF can be harnessed across a wide range of machine learning applications, including unconditional/conditional image generation, style transfer, and audio-text translation. To further enhance model efficiency on high-dimensional image datasets, a two-phase NSGF++ model is devised, which first follows the Sinkhorn flow to approach the image manifold quickly (≤ 5 NFEs) and then refine the samples along a simple straight flow. A novel phase-transition time predictor is proposed to transfer between the two phases.

We empirically validate NSGF on low-dimensional 2D data and NSGF++ on benchmark images (MNIST, CIFAR-10). Our findings indicate that our models can be trained to yield commendable results in terms of generation cost and sample quality, surpassing the performance of the neural Wasserstein gradient flow methods previously tested on CIFAR-10, to the best of our knowledge.

2 Related Works

Sinkhorn Divergence in Machine Learning. Originally introduced in the domain of optimal transport, the Sinkhorn divergence emerged as a more computationally tractable alternative to the classical Wasserstein distance [Cuturi, 2013; Peyré *et al.*, 2017; Feydy *et al.*, 2019]. Since its inception, Sinkhorn divergence has found applications across a range of machine learning tasks, including domain adaptation [Alaya *et al.*, 2019; Komatsu *et al.*, 2021], Sinkhorn barycenter [Luise *et al.*, 2019; Shen *et al.*, 2020] and color transfer [Pai *et al.*, 2021]. Indeed, it has already been extended to single-step generative modeling methods, such as the Sinkhorn GAN and VAE [Genevay *et al.*, 2018; Deja *et al.*, 2020; Patrini *et al.*, 2020]. However, to the best of our knowledge, it has yet to be employed in developing efficient generative Wasserstein gradient flow models.

Neural ODE/SDE Based Diffusion Models. Recently, diffusion models, as a class of Neural ODE/SDE Based generative methods have achieved unprecedented success, which also transforms a simple density to the target distribution, iteratively [Song and Ermon, 2019; Ho *et al.*, 2020; Song *et al.*, 2021]. Typically, each step of diffusion models only progresses a little by denoising a simple Gaussian noise, while each step in WGF models follows the most informative direction (in a certain sense). Hence, diffusion models usually have a long inference trajectory. In recent research undertakings, there has been a growing interest in exploring more informative steps within diffusion models. Specifically, flow matching methods [Lipman *et al.*, 2023; Liu *et al.*, 2023; Albergo and Vanden-Eijnden, 2023] establish correspondence between the source and target via optimal transport, subsequently crafting a probability path by directly linking data points from both ends. Notably, when the source and target are both Gaussians, their path is actually a Wasserstein gradient flow. However, this property does not consistently hold for general data probabilities. Moreover, [Tong *et al.*, 2023; Pooladian *et al.*, 2023] consider calculating the minibatch op-

timal transport map to guide data points connecting. Besides, [Das *et al.*, 2023] consider the shortest forward diffusion path for the Fisher metric and [Shaul *et al.*, 2023] explore the conditional Gaussian probability path based on the principle of minimizing the Kinetic Energy. Nonetheless, a commonality among many of these methods is their reliance on Gaussian paths for theoretical substantiation, thereby constraining the broader applicability of these techniques within real-world generative modeling.

3 Preliminaries

3.1 Notations

We denote $\mathbf{x} = (x_1, \dots, x_d) \in \mathbb{R}^d$ and $\mathcal{X} \subset \mathbb{R}^d$ as a vector and a compact ground set in \mathbb{R}^d , respectively. For a given point $\mathbf{x} \in \mathcal{X}$, $\|\mathbf{x}\|_p := (\sum_i x_i^p)^{\frac{1}{p}}$ denotes the p -norm on Euclidean space, and $\delta_{\mathbf{x}}$ stands for the Dirac (unit mass) distribution at point $\mathbf{x} \in \mathcal{X}$. $\mathcal{P}_2(\mathcal{X})$ denotes the set of probability measures on \mathcal{X} with finite second moment and $\mathcal{C}(\mathcal{X})$ denotes the space of continuous functions on \mathcal{X} . For a given functional $\mathcal{F}(\cdot) : \mathcal{P}_2(\mathcal{X}) \rightarrow \mathbb{R}$, $\frac{\delta \mathcal{F}(\mu_t)}{\delta \mu}(\cdot) : \mathbb{R}^d \rightarrow \mathbb{R}$ denotes its first variation at $\mu = \mu_t$. Besides, we use ∇ and $\nabla \cdot (\cdot)$ to denote the gradient and the divergence operator, respectively.

3.2 Wasserstein distance and Sinkhorn divergence

We first introduce the background of Wasserstein distance. Given two probability measures $\mu, \nu \in \mathcal{P}_2(\mathcal{X})$, the p -Wasserstein distance $\mathcal{W}_p(\mu, \nu) : \mathcal{P}_2(\mathcal{X}) \times \mathcal{P}_2(\mathcal{X}) \rightarrow \mathbb{R}_+$ is defined as:

$$\mathcal{W}_p(\mu, \nu) = \inf_{\pi \in \Pi(\mu, \nu)} \left(\int_{\mathcal{X} \times \mathcal{X}} \|\mathbf{x} - \mathbf{y}\|^p d\pi(\mathbf{x}, \mathbf{y}) \right)^{\frac{1}{p}}, \quad (1)$$

where $\Pi(\mu, \nu)$ denotes the set of all probability couplings π with marginals μ and ν . The \mathcal{W}_p distance aims to find a coupling π so as to minimize the cost function $\|\mathbf{x} - \mathbf{y}\|^p$ of moving a probability mass from μ to ν . It has been demonstrated that the p -Wasserstein distance is a valid metric on $\mathcal{P}_2(\mathcal{X})$, and $(\mathcal{P}_2(\mathcal{X}), \mathcal{W}_p)$ is referred to as the Wasserstein probability space [Villani and others, 2009].

Note that directly calculating \mathcal{W}_p is computationally expensive, especially for high dimensional problems [Santambrogio, 2015]. Consequently, the entropy-regularized Wasserstein distance [Cuturi, 2013] is proposed to approximate equation 1 by regularizing the original problem with an entropy term:

Definition 1. *The entropy-regularized Wasserstein distance is formally defined as:*

$$\begin{aligned} \mathcal{W}_{p,\varepsilon}(\mu, \nu) &= \\ &\inf_{\pi \in \Pi(\mu, \nu)} \left[\left(\int_{\mathcal{X} \times \mathcal{X}} \|\mathbf{x} - \mathbf{y}\|^p d\pi(\mathbf{x}, \mathbf{y}) \right)^{\frac{1}{p}} + \varepsilon KL(\pi \| \mu \otimes \nu) \right], \end{aligned} \quad (2)$$

where $\varepsilon > 0$ is a regularization coefficient, $\mu \otimes \nu$ denotes the product measure, i.e., $\mu \otimes \nu(\mathbf{x}, \mathbf{y}) = \mu(\mathbf{x})\nu(\mathbf{y})$, and $KL(\pi \| \mu \otimes \nu)$ denotes the KL-divergence between π and $\mu \otimes \nu$.

Generally, the computational cost of $\mathcal{W}_{p,\varepsilon}$ is much lower than \mathcal{W}_p , and can be efficiently calculated with Sinkhorn algorithms [Cuturi, 2013]. Without loss of generality, we fix

$p = 2$ and abbreviate $\mathcal{W}_{2,\varepsilon} := \mathcal{W}_\varepsilon$ for ease of notion in the whole paper. According to Fenchel-Rockafellar theorem, the entropy-regularized Wasserstein problem \mathcal{W}_ε equation 2 has an equivalent dual formulation, which is given as follows [Peyré *et al.*, 2017]:

$$\begin{aligned} \mathcal{W}_\varepsilon(\mu, \nu) &= \max_{f, g \in \mathcal{C}(\mathcal{X})} \langle \mu, f \rangle + \langle \nu, g \rangle \\ &\quad - \varepsilon \left\langle \mu \otimes \nu, \exp \left(\frac{1}{\varepsilon} (f \oplus g - C) \right) - 1 \right\rangle, \end{aligned} \quad (3)$$

where C is the cost function in equation 2 and $f \oplus g$ is the tensor sum: $(x, y) \in \mathcal{X}^2 \mapsto f(x) + g(y)$. The maximizers $f_{\mu, \nu}$ and $g_{\mu, \nu}$ of equation 3 are called the \mathcal{W}_ε -potentials of $\mathcal{W}_\varepsilon(\mu, \nu)$. The following lemma states the optimality condition for the \mathcal{W}_ε -potentials:

Lemma 1. *(Optimality [Cuturi, 2013]) The \mathcal{W}_ε -potentials $(f_{\mu, \nu}, g_{\mu, \nu})$ exist and are unique (μ, ν)—a.e. up to an additive constant (i.e. $\forall K \in \mathbb{R}, (f_{\mu, \nu} + K, g_{\mu, \nu} - K)$ is optimal). Moreover,*

$$\mathcal{W}_\varepsilon(\mu, \nu) = \langle \mu, f_{\mu, \nu} \rangle + \langle \nu, g_{\mu, \nu} \rangle. \quad (4)$$

We describe such the method in Appendix A for completeness. Note that, although computationally more efficient than the \mathcal{W}_p distance, the \mathcal{W}_ε distance is not a true metric, as there exists $\mu \in \mathcal{P}_2(\mathcal{X})$ such that $\mathcal{W}_\varepsilon(\mu, \mu) \neq 0$ when $\varepsilon \neq 0$, which restricts the applicability of \mathcal{W}_ε . As a result, the following Sinkhorn divergence $\mathcal{S}_\varepsilon(\mu, \nu) : \mathcal{P}_2(\mathcal{X}) \times \mathcal{P}_2(\mathcal{X}) \rightarrow \mathbb{R}$ is proposed [Peyré *et al.*, 2017]:

Definition 2. *Sinkhorn divergence:*

$$\mathcal{S}_\varepsilon(\mu, \nu) = \mathcal{W}_\varepsilon(\mu, \nu) - \frac{1}{2} (\mathcal{W}_\varepsilon(\mu, \mu) + \mathcal{W}_\varepsilon(\nu, \nu)). \quad (5)$$

$\mathcal{S}_\varepsilon(\mu, \nu)$ is nonnegative, bi-convex thus a valid metric on $\mathcal{P}_2(\mathcal{X})$ and metricize the convergence in law. Actually $\mathcal{S}_\varepsilon(\mu, \nu)$ interpolates the Wasserstein distance ($\varepsilon \rightarrow 0$) and the Maximum Mean Discrepancy ($\varepsilon \rightarrow \infty$) [Feydy *et al.*, 2019].

3.3 Gradient flows

Consider an optimization problem over $\mathcal{P}_2(\mathcal{X})$:

$$\min_{\mu \in \mathcal{P}_2(\mathcal{X})} \mathcal{F}(\mu) := \mathcal{D}(\mu \| \mu^*). \quad (6)$$

where μ^* is the target distribution, \mathcal{D} is the divergence we choose. We consider now the problem of transporting mass from an initial distribution μ_0 to a target distribution μ^* , by finding a continuous probability path μ_t starting from $\mu_0 = \mu$ that converges to μ^* while decreasing $\mathcal{F}(\mu_t)$. To solve this optimization problem, one can consider a descent flow of $\mathcal{F}(\mu)$ in the Wasserstein space, which transports any initial distribution μ_0 towards the target distribution μ^* . Specifically, the descent flow of $\mathcal{F}(\mu)$ is described by the following continuity equation [Ambrosio *et al.*, 2005; Villani and others, 2009; Santambrogio, 2017]:

$$\frac{\partial \mu_t(x)}{\partial t} = -\nabla \cdot (\mu_t(x) \mathbf{v}_t(x)). \quad (7)$$

where $\mathbf{v}_{\mu_t} : \mathcal{X} \rightarrow \mathcal{X}$ is a velocity field that defines the direction of position transportation. To ensure a descent of $\mathcal{F}(\mu_t)$

over time t , the velocity field \mathbf{v}_{μ_t} should satisfy the following inequality ([Ambrosio *et al.*, 2005]):

$$\frac{d\mathcal{F}(\mu_t)}{dt} = \int \langle \nabla \frac{\delta\mathcal{F}(\mu_t)}{\delta\mu}, \mathbf{v}_t \rangle d\mu_t \leq 0. \quad (8)$$

A straightforward choice of \mathbf{v}_t is $\mathbf{v}_t = -\nabla \frac{\delta\mathcal{F}(\mu_t)}{\delta\mu}$, which is actually the steepest descent direction of $\mathcal{F}(\mu_t)$. When we select this \mathbf{v}_t , we refer to the aforementioned continuous equation as the *Wasserstein gradient flow* of \mathcal{F} . We give the definition of the first variation in the appendix for the sake of completeness of the article.

4 Methodology

In this section, we first introduce the Sinkhorn Wasserstein gradient flow and investigate its convergence properties. Then, we develop our Neural Sinkhorn Gradient Flow model, which consists of a velocity field matching training procedure and a velocity field guided inference procedure. Moreover, we theoretically show that the mean-field limit of the empirical approximation used in the training procedure converges to the true velocity field of the Sinkhorn Wasserstein gradient flow.

4.1 Sinkhorn Wasserstein gradient flow

Based on the definition of the Sinkhorn divergence, we construct our Sinkhorn objective $\mathcal{F}_\varepsilon(\cdot) = \mathcal{S}_\varepsilon(\cdot, \mu^*)$, where μ^* denotes the target distribution. The following theorem gives the first variation of the Sinkhorn objective.

Theorem 1. (First variation of the Sinkhorn objective [Luise et al., 2019]) Let $\varepsilon > 0$. Let $(f_{\mu, \mu^*}, g_{\mu, \mu^*})$ be the \mathcal{W}_ε -potentials of $\mathcal{W}_\varepsilon(\mu, \mu^*)$ and $(f_{\mu, \mu}, g_{\mu, \mu})$ be the \mathcal{W}_ε -potentials of $\mathcal{W}_\varepsilon(\mu, \mu)$. The first variation of the Sinkhorn objective \mathcal{F}_ε is

$$\frac{\delta\mathcal{F}_\varepsilon}{\delta\mu} = f_{\mu, \mu^*} - f_{\mu, \mu}. \quad (9)$$

According to Theorem 1, we can construct the Sinkhorn Wasserstein gradient flow by setting the velocity field \mathbf{v}_t in the continuity equation equation 7 as $\mathbf{v}_{\mu_t}^{\mathcal{F}_\varepsilon} = -\nabla \frac{\delta\mathcal{F}_\varepsilon(\mu_t)}{\delta\mu_t} = \nabla f_{\mu_t, \mu_t} - \nabla f_{\mu_t, \mu^*}$.

Proposition 1. Consider the Sinkhorn Wasserstein gradient flow described by the following continuity equation:

$$\frac{\partial\mu_t(\mathbf{x})}{\partial t} = -\nabla \cdot (\mu_t(\mathbf{x})(\nabla f_{\mu_t, \mu_t}(\mathbf{x}) - \nabla f_{\mu_t, \mu^*}(\mathbf{x}))). \quad (10)$$

The following local descending property of \mathcal{F}_ε holds:

$$\frac{d\mathcal{F}_\varepsilon(\mu_t)}{dt} = - \int \|\nabla f_{\mu_t, \mu_t}(\mathbf{x}) - \nabla f_{\mu_t, \mu^*}(\mathbf{x})\|^2 d\mu_t, \quad (11)$$

where the r.h.s. equals 0 if and only if $\mu_t = \mu^*$.

4.2 Velocity-fields Matching

We now present our NSGF method, the core of which lies in training a neural network to approximate the time-varying velocity field $\mathbf{v}_{\mu_t}^{\mathcal{F}_\varepsilon}$ induced by Sinkhorn Wasserstein gradient flow. Given a target probability density path $\mu_t(x)$ and it's

corresponding velocity field $\mathbf{v}_{\mu_t}^{\mathcal{S}_\varepsilon}$, which generates $\mu_t(x)$, we define the velocity field matching objective as follows:

$$\min_\theta \mathbf{E}_{t \sim [0, T], x \sim \mu_t} \left[\|\mathbf{v}^\theta(x, t) - \mathbf{v}_{\mu_t}^{\mathcal{S}_\varepsilon}(x)\|^2 \right]. \quad (12)$$

To construct our algorithm, we utilize independently and identically distributed (i.i.d) samples denoted as $\{Y_i\}_{i=1}^n \in \mathbb{R}^d$, which are drawn from an unknown target distribution μ^* a common practice in the field of generative modeling. Given the current set of samples $\{\tilde{X}_i^t\}_{i=1}^n \sim \mu_t$, our method calculates the velocity field using the \mathcal{W}_ε -potentials (Lemma 1) $f_{\tilde{\mu}_t, \tilde{\mu}^*}$ and $f_{\tilde{\mu}_t, \tilde{\mu}_t}$ based on samples. Here, $\tilde{\mu}_t$ and $\tilde{\mu}^*$ represent discrete Dirac distributions.

Remark 1. In the discrete case, \mathcal{W}_ε -potentials equation 1 can be computed by a standard method in [Genevay et al., 2016]. In practice, we use the efficient implementation of the Sinkhorn algorithm with GPU acceleration from the Geom-Loss package [Feydy et al., 2019].

The corresponding finite sample velocity field approximation can be computed as follows:

$$\hat{\mathbf{v}}_{\tilde{\mu}_t}^{\mathcal{F}_\varepsilon}(\tilde{X}_i^t) = \nabla_{\tilde{X}_i^t} f_{\tilde{\mu}_t, \tilde{\mu}_t}(\tilde{X}_i^t) - \nabla_{\tilde{X}_i^t} f_{\tilde{\mu}_t, \tilde{\mu}^*}(\tilde{X}_i^t). \quad (13)$$

Subsequently, we derive the particle formulation corresponding to the flow formulation equation 10.

$$d\tilde{X}_i^t = \hat{\mathbf{v}}_{\tilde{\mu}_t}^{\mathcal{F}_\varepsilon}(\tilde{X}_i^t) dt, i = 1, 2, \dots, n. \quad (14)$$

In the following proposition, we investigate the mean-field limit of the particle set $\{\tilde{X}_i^t\}_{i=1, \dots, M}$.

Theorem 2. (Mean-field limits.) Suppose the empirical distribution $\tilde{\mu}_0$ of M particles weakly converges to a distribution μ_0 when $M \rightarrow \infty$. Then, the path of equation equation 14 starting from $\tilde{\mu}_0$ weakly converges to a solution of the following partial differential equation starting from μ_0 when $M \rightarrow \infty$:

$$\frac{\partial\mu_t(x)}{\partial t} = -\nabla \cdot (\mu_t(x) \nabla \frac{\delta\mathcal{F}_\varepsilon(\mu_t)}{\delta\mu_t}). \quad (15)$$

which is actually the gradient flow of Sinkhorn divergence \mathcal{F}_ε in the Wasserstein space.

The following proposition shows that the goal of the velocity field matching objective equation 12 can be regarded as approximating the steepest local descent direction with neural networks.

Proposition 2. (Steepest local descent direction.) Consider the infinitesimal transport $T(x) = x + \lambda\phi$. The Fréchet derivative under this particular perturbation,

$$\begin{aligned} \frac{d}{d\lambda} \mathcal{F}_\varepsilon(T_\# \mu)|_{\lambda=0} &= \lim_{\lambda \rightarrow 0} \frac{\mathcal{F}_\varepsilon(T_\# \mu) - \mathcal{F}_\varepsilon(\mu)}{\lambda} \\ &= \int_{\mathcal{X}} \nabla f_{\mu, \mu^*}(\mathbf{x}) \phi(\mathbf{x}) d\mu - \int_{\mathcal{X}} \nabla f_{\mu, \mu}(\mathbf{x}) \phi(\mathbf{x}) d\mu, \end{aligned} \quad (16)$$

and the steepest local descent direction is $\phi = \frac{\nabla f_{\mu, \mu^*}(\mathbf{x}) - f_{\mu, \mu}(\mathbf{x})}{\|\nabla f_{\mu, \mu^*}(\mathbf{x}) - f_{\mu, \mu}(\mathbf{x})\|}$.

Algorithm 1: Velocity field matching training

Input : number of time steps T , batch size n , gradient flow step size $\eta > 0$, empirical or samplable distribution μ_0 and μ^* , neural network parameters θ , optimizer step size $\gamma > 0$

```

/* Build trajectory pool */
while Building do
    /* Sample batches of size  $n$  i.i.d. from the datasets */
     $\tilde{X}_i^0 \sim \mu_0, \tilde{Y}_i \sim \mu^*, i = 1, 2, \dots, n.$ 
    for  $t = 0, 1, \dots, T$  do
        calculate  $f_{\tilde{\mu}_t, \tilde{\mu}_t}(\tilde{X}_i^t), f_{\tilde{\mu}_t, \tilde{\mu}^*}(\tilde{X}_i^t)$ .
         $\hat{v}_{\mu_t}^{\mathcal{F}_\epsilon}(\tilde{X}_i^t) = \nabla f_{\tilde{\mu}_t, \tilde{\mu}_t}(\tilde{X}_i^t) - \nabla f_{\tilde{\mu}_t, \tilde{\mu}^*}(\tilde{X}_i^t).$ 
         $\tilde{X}_i^{t+1} = \tilde{X}_i^t + \eta \hat{v}_t^{\mathcal{F}_\epsilon}(\tilde{X}_i^t).$ 
        store all  $(\tilde{X}_i^t, \hat{v}_t^{\mathcal{F}_\epsilon}(\tilde{X}_i^t))$  pair into the pool,  $i = 1, 2, \dots, n.$ 
    /* velocity field matching */
    while Not convergence do
        from trajectory pool sample pair  $(\tilde{X}_i^t, \hat{v}_t^{\mathcal{F}_\epsilon}(\tilde{X}_i^t)).$ 
         $\mathcal{L}(\theta) = \|v^\theta(\tilde{X}_i^t, t) - \hat{v}_{\mu_t}^{\mathcal{F}_\epsilon}(\tilde{X}_i^t)\|^2,$ 
         $\theta \leftarrow \theta - \gamma \nabla_\theta \mathcal{L}(\theta).$ 
Output:  $\theta$  parameterize the time-varying velocity field

```

Algorithm 2: Inference via velocity field

Input : number of time steps T , inference step size η , time-varying velocity field v^θ , prior samples $\tilde{X}_i^0 \sim \tilde{\mu}_0$

```

for  $t = 0, 1, \dots, T$  do
     $\tilde{X}_i^{t+1} = \tilde{X}_i^t + \eta v^\theta(\tilde{X}_i^t, t), i = 1, 2, \dots, n.$ 
Output:  $\tilde{X}_i^T$  as the results.

```

4.3 Minibatch Sinkhorn Gradient Flow and Experience Replay

According to Theorem 2, we construct our NSGF method based on minibatches. We utilize a set of discrete targets, denoted as $\{Y_i\}_{i=1}^n$, where n represents the batch size, to construct the Sinkhorn Gradient Flow starting from random Gaussian noise or other initial distributions. As indicated by Theorem 2, the mean-field limit converges to the true Sinkhorn Gradient flow when the batch size approaches ∞ . Note that in practice, we only use a moderate batch size for computation efficiency, and the experimental results demonstrate that this works well for practical generative tasks.

Considering the balance between expensive training costs and training quality, we opted to first build a trajectory pool of Sinkhorn gradient flow and then sample from it to construct the velocity field matching algorithm. Our method draws inspiration from experience replay, a common technique in reinforcement learning, adapting it to enhance our model’s effectiveness [Mnih *et al.*, 2013; Silver *et al.*, 2016]. Once we calculate the time-varying velocity field $\hat{v}_{\mu_t}^s(\tilde{X}_i^t)$, we can parameterize the velocity field using a straightforward regression method. The velocity field matching training procedure is outlined in Algorithm 1.

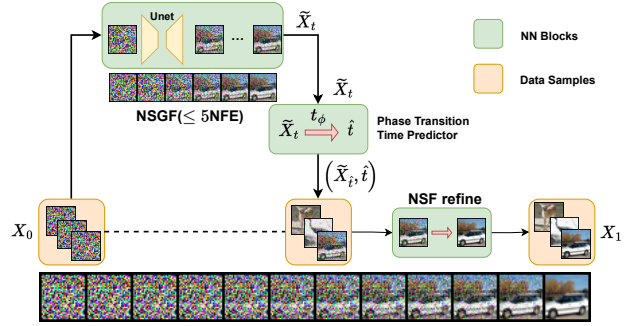


Figure 2: NSGF++ framework

Once obtained a feasible velocity field approximation v^θ , one can generate new samples by iteratively employing the explicit Euler discretization of the Equation equation 14 to drive the samples to the target. Note that various other numerical schemes, such as the implicit Euler method [Platen and Bruti-Liberati, 2010] and Runge-Kutta methods [Butcher, 1964], can be employed. In this study, we opt for the first-order explicit Euler discretization method [Süli and Mayers, 2003] due to its simplicity and ease of implementation. We leave the exploration of higher-order algorithms for future research.

4.4 NSGF++

In this subsection, we propose an approach to enhance the performance of NSGF on high-dimensional datasets. As a trajectory pool should be first constructed in the velocity field matching training procedure of NSGF, the storage and computation costs would greatly hinder the usage of NSGF in large-scale tasks. To tackle this problem, we propose a two-phase NSGF++ algorithm, which first follows the Sinkhorn gradient flow to approach the image manifold quickly and then refine the samples along a simple straight flow. Specifically, our NSGF++ model consists of three components, (1) a NSGF model trained on $T \leq 5$ time steps, (2) a Neural Straight Flow (NSF) model trained via velocity field matching on a straight flow $X_t \sim (1-t)P_0 + tP_1, t \in [0, 1]$, which has also been used in existing FM models, (3) a phase-transition time predictor to transfer from NSGF to the NSF. Here, we train the time predictor $t_\phi : \mathcal{X} \rightarrow [0, 1]$ with the following regression objective:

$$L(\phi) = E_{t \in \mathcal{U}(0,1), X_t \sim P_t} \|t - t_\phi(X_t)\|^2.$$

Note that the training of the straight NSF model and the time predictor is simulated free and need no extra storage. As a result, the training cost of NSGF++ is similar to existing FM models, since the computation cost of NSF is nearly the same as FM, and the 5-step NSGF and the time predictor is easy to train.

In the inference of NSGF++, we first follow the NSGF with less than 5 NFEs form $X_0 \sim P_0$ to obtain \tilde{X}_t , then transfer it with the time predictor t_ϕ , and obtain our final output by refining the transferred sample with the NSF model from $t_\phi(\tilde{X}_t)$, as shown in Figure 5.

Algorithm	2-Wasserstein distance (10 steps)					2-Wasserstein distance (100 steps)				
	8gaussians	8gaussians-moons	moons	scurve	checkerboard	8gaussians	8gaussians-moons	moons	scurve	checkerboard
NSGF (ours)	0.285	0.144	0.077	0.117	0.252	0.278	0.144	0.067	0.110	0.147
JKO-Flow	0.290	0.177	0.085	0.135	0.269	0.274	0.167	0.085	0.123	0.160
EPT	0.295	0.180	0.082	0.138	0.277	0.289	0.176	0.080	0.118	0.163
OT-CFM	0.289	0.173	0.088	0.149	0.253	0.269	0.165	0.078	0.127	0.159
1-RF	0.427	0.294	0.107	0.169	0.396	0.415	0.293	0.099	0.136	0.166
2-RF	0.428	0.311	0.125	0.171	0.421	0.430	0.311	0.121	0.136	0.170
3-RF	0.421	0.298	0.110	0.170	0.413	0.414	0.297	0.103	0.140	0.170
SI	0.435	0.324	0.134	0.187	0.427	0.411	0.294	0.096	0.139	0.166
FM	0.423	0.292	0.111	0.171	0.417	0.415	0.290	0.097	0.135	0.165

Table 1: Comparison of neural gradient-flow-based methods and neural ODE-based diffusion models over five data sets with 10/100 Euler steps. The principle of steps in JKO-flow means backward Eulerian method steps (JKO steps).

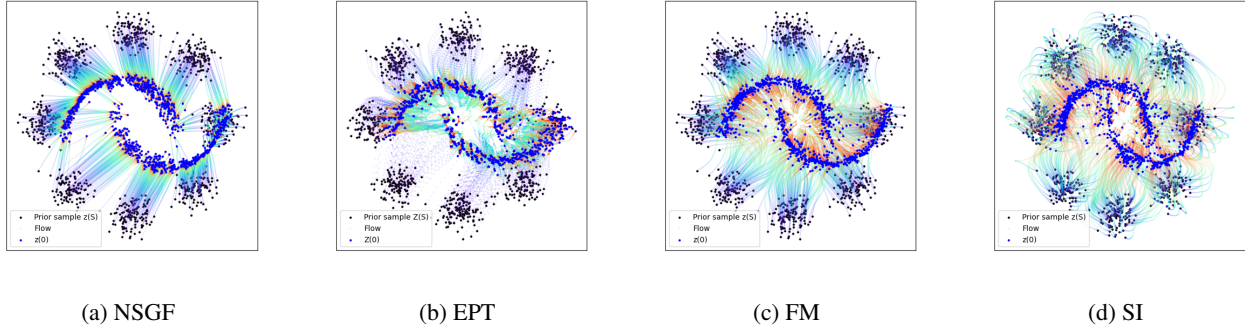


Figure 3: Visualization results for 2D generated paths. We show different methods that drive the particle from the prior distribution (black) to the target distribution (blue). The color change of the flow shows the different number of steps (from blue to red means from 0 to T).

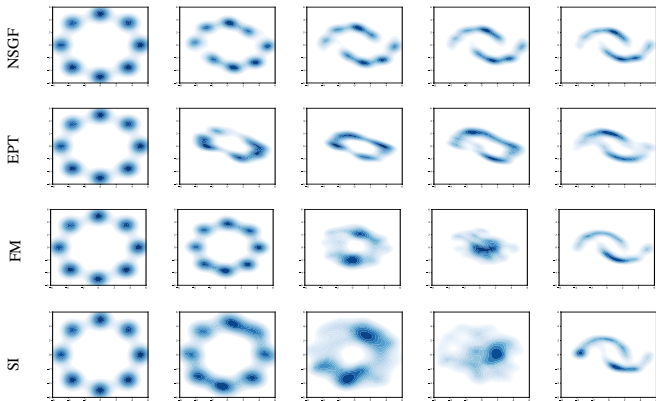


Figure 4: 2-Wasserstein Distance of the generated process utilizing neural ODE-based diffusion models and NSGF. The FM/SI methods reduce noise roughly linearly, while NSGF quickly recovers the target structure and progressively optimizes the details in subsequent steps.

5 Experiments

We conduct an empirical investigation of the NSGF-based generative models (the standard NSGF and its two-phase variant NSGF++) across a range of experiments. Initially, we demonstrate how NSGF guides the evolution and convergence of particles from the initial distribution toward the target distribution in 2D simulation experiments. Subsequently, our attention turns to real-world image benchmarks, such as MNIST and CIFAR-10. To improve the efficiency in those high-dimensional tasks, we adopt the two-phase variant NSGF++ instead of the standard NSGF. Our method’s adapt-

ability to high-dimensional spaces is exemplified through experiments conducted on these datasets.

5.1 2D simulation data

We assess the performance of various generative modeling models in low dimensions. Specifically, we conduct a comparative analysis between our method, NSGF, and several neural ODE-based diffusion models, including Flow Matching (FM; [Lipman *et al.*, 2023]), Rectified Flow (1,2,3-RF; [Liu *et al.*, 2023]), Optimal Transport Condition Flow Matching (OT-CFM; [Tong *et al.*, 2023; Pooladian *et al.*, 2023]), Stochastic Interpolant (SI; [Albergo and Vanden-Eijnden, 2023]), and neural gradient-flow-based models such as JKO-Flow [Fan *et al.*, 2022] and EPT [Gao *et al.*, 2022]. Our evaluation involves learning 2D distributions adapted from [Grathwohl *et al.*, 2018], which include multiple modes.

Table 1 provides a comprehensive overview of our 2D experimental results, clearly illustrating the generalization capabilities of NSGF. Even when employing fewer steps. It is evident that neural gradient-flow-based models consistently outperform neural ODE-based diffusion models, particularly in low-step settings. This observation suggests that neural gradient-flow-based models generate more informative paths, enabling effective generation with a reduced number of steps. Furthermore, our results showcase the best performances among neural gradient-flow-based models, indicating that we have successfully introduced a lower error in approximating Wasserstein gradient flows. More complete details of the experiment can be found in the appendix E. In the absence of specific additional assertions, we adopted Euler steps as the inference steps.

Algorithm	CIFAR 10		
	IS(\uparrow)	FID(\downarrow)	NFE(\downarrow)
NSGF++ (ours)	8.86	5.55	59
EPT[2022]	/	46.63	10k
JKO-Flow[2022]	7.48	23.7	>150
DGGF[2022]	/	28.12	110
OT-CFM[2023]	/	11.14	100
FM[2023]	/	6.35	142
RF[2023]	9.20	4.88	100
SI[2023]	/	10.27	/

Table 2: Comparison of Neural Wasserstein gradient flow methods and Neural ODE-based diffusion models over CIFAR-10

We present additional comparisons between neural ODE-based diffusion models and neural gradient-flow-based models, represented by NSGF and EPT, in Figure 3, 4, which illustrates the flow at different steps from 0 to T . Our observations reveal that the velocity field induced by NSGF exhibits notably high-speed values right from the outset. This is attributed to the fact that NSGF follows the steepest descent direction within the probability space. In contrast, neural ODE-based diffusion models, particularly those based on stochastic interpolation, do not follow the steepest descent path in 2D experiments. Even with the proposed rectified flow method by [Liu *et al.*, 2023] to straighten the path, these methods still necessitate more steps to reach the desired outcome.

5.2 Image benchmark data

In this section, we illustrate the scalability of our algorithm to the high-dimensional setting by applying our methods to real image datasets. Notably, we leverage the two-phase variant (NSGF++) instead of the standard NSGF to enhance efficiency in high-dimensional spaces. It is worth mentioning that we achieve this improvement by constructing a significantly smaller training pool compared with the standard NSGF pool (10% of the usual size), thus requiring only 5% of the typical training duration. We evaluate NSGF++ on MNIST and CIFAR10 to show our generating ability. Due to the limit of the space, we defer the generative images and comparison results of MNIST in appendix 3.

We report sample quality using the standard Fréchet Inception Distance (FID) [Heusel *et al.*, 2017], Inception Score (IS) [Salimans *et al.*, 2016] and compute cost using the number of function evaluations (NFE). These are all standard metrics throughout the literature.

Table 2 presents the results, including the Fréchet Inception Distance (FID), Inception Score (IS), and the number of function evaluations (NFE), comparing the empirical distribution generated by each algorithm with the target distribution. While our current implementation may not yet rival state-of-the-art methods, it demonstrates promising outcomes, particularly in terms of generating quality (FID), outperforming neural gradient-flow-based models (EPT, [Gao *et al.*, 2022]; JKO-Flow, [Fan *et al.*, 2022]; DGGF, (LSIF- \mathcal{X}^2) [Heng *et al.*, 2022]) with fewer steps. It's essential to emphasize that this work represents an initial exploration of this particular model category and has not undergone optimization



Figure 5: The inference result of our NSGF++ model. The first row shows the result after 5 NSGF steps and the second row shows the final results.

using common training techniques found in recent diffusion-based approaches. Such techniques include the use of exponential moving averages, truncations, learning rate warm-ups, and similar strategies. Furthermore, it's worth noting that training neural gradient-flow-based models like NSGF in high-dimensional spaces can be challenging. Balancing the optimization of per-step information with the limitations of the neural network's expressive power presents an intriguing research avenue that warrants further investigation.

6 Conclusion

This paper delves into the realm of Wasserstein gradient flow w.r.t. the Sinkhorn divergence as an alternative to kernel methods. Our main investigation revolves around the Neural Sinkhorn Gradient Flow (NSGF) model, which introduces a parameterized velocity field that evolves over time in the Sinkhorn gradient flow. One noteworthy aspect of the NSGF is its efficient velocity field matching, which relies solely on samples from the target distribution for empirical approximations. The combination of rigorous theoretical foundations and empirical observations demonstrates that our approximations of the velocity field converge toward their true counterparts as the sample sizes grow. To further enhance model efficiency on high-dimensional tasks, a two-phase NSGF++ model is devised, which first follows the Sinkhorn flow to approach the image manifold quickly and then refine the samples along a simple straight flow. Through extensive empirical experiments on well-known datasets like MNIST and CIFAR-10, we validate the effectiveness of the proposed methods.

References

- [Alaya *et al.*, 2019] Mokhtar Z Alaya, Maxime Berar, Gilles Gasso, and Alain Rakotomamonjy. Screening sinkhorn algorithm for regularized optimal transport. *NeurIPS*, 32, 2019.
- [Albergo and Vanden-Eijnden, 2023] Michael Samuel Albergo and Eric Vanden-Eijnden. Building normalizing flows with stochastic interpolants. In *The Eleventh ICLR*, 2023.
- [Alvarez-Melis *et al.*, 2022] David Alvarez-Melis, Yair Schiff, and Youssef Mroueh. Optimizing functionals on the space of probabilities with input convex neural networks. *Transactions on Machine Learning Research*, 2022.
- [Ambrosio *et al.*, 2005] Luigi Ambrosio, Nicola Gigli, and Giuseppe Savaré. *Gradient flows: in metric spaces and in the space of probability measures*. Springer Science & Business Media, 2005.
- [Amos *et al.*, 2017] Brandon Amos, Lei Xu, and J Zico Kolter. Input convex neural networks. In *ICML*, pages 146–155. PMLR, 2017.
- [Ansari *et al.*, 2021] Abdul Fatir Ansari, Ming Liang Ang, and Harold Soh. Refining deep generative models via discriminator gradient flow. In *ICLR*, 2021.
- [Arbel *et al.*, 2019] Michael Arbel, Anna Korba, Adil Salim, and Arthur Gretton. Maximum mean discrepancy gradient flow. *NeurIPS*, 32, 2019.
- [Bunne *et al.*, 2022] Charlotte Bunne, Laetitia Papaxanthos, Andreas Krause, and Marco Cuturi. Proximal optimal transport modeling of population dynamics. In *International Conference on Artificial Intelligence and Statistics*, pages 6511–6528. PMLR, 2022.
- [Butcher, 1964] John C Butcher. Implicit runge-kutta processes. *Mathematics of computation*, 18(85):50–64, 1964.
- [Choi *et al.*, 2022] Kristy Choi, Chenlin Meng, Yang Song, and Stefano Ermon. Density ratio estimation via infinitesimal classification. In *International Conference on Artificial Intelligence and Statistics*, pages 2552–2573. PMLR, 2022.
- [Cuturi, 2013] Marco Cuturi. Sinkhorn distances: Lightspeed computation of optimal transport. *NeurIPS*, 26, 2013.
- [Dai and Seljak, 2020] Biwei Dai and Uros Seljak. Sliced iterative normalizing flows. *arXiv preprint arXiv:2007.00674*, 2020.
- [Damodaran *et al.*, 2018] Bharath Bhushan Damodaran, Benjamin Kellenberger, Rémi Flamary, Devis Tuia, and Nicolas Courty. Deepjdot: Deep joint distribution optimal transport for unsupervised domain adaptation. In *Proceedings of the European conference on computer vision (ECCV)*, pages 447–463, 2018.
- [Das *et al.*, 2023] Ayan Das, Stathi Fotiadis, Anil Batra, Farhang Nabiei, FengTing Liao, Sattar Vakili, Da-shan Shiu, and Alberto Bernacchia. Image generation with shortest path diffusion. *arXiv preprint arXiv:2306.00501*, 2023.
- [Deja *et al.*, 2020] Kamil Deja, Jan Dubiński, Piotr Nowak, Sandro Wenzel, Przemysław Spurek, and Tomasz Trzcinski. End-to-end sinkhorn autoencoder with noise generator. *IEEE Access*, 9:7211–7219, 2020.
- [Dhariwal and Nichol, 2021] Prafulla Dhariwal and Alexander Nichol. Diffusion models beat gans on image synthesis. *Advances in neural information processing systems*, 34:8780–8794, 2021.
- [Du *et al.*, 2023] Chao Du, Tianbo Li, Tianyu Pang, YAN Shuicheng, and Min Lin. Nonparametric generative modeling with conditional sliced-wasserstein flows. 2023.
- [Fan *et al.*, 2022] Jiaoqiao Fan, Qinsheng Zhang, Amirhossein Taghvaei, and Yongxin Chen. Variational wasserstein gradient flow. In *ICML*, pages 6185–6215. PMLR, 2022.
- [Fatras *et al.*, 2019] Kilian Fatras, Younes Zine, Rémi Flamary, Rémi Gribonval, and Nicolas Courty. Learning with minibatch wasserstein: asymptotic and gradient properties. *arXiv preprint arXiv:1910.04091*, 2019.
- [Fatras *et al.*, 2021a] Kilian Fatras, Thibault Séjourné, Rémi Flamary, and Nicolas Courty. Unbalanced minibatch optimal transport: applications to domain adaptation. In *ICML*, pages 3186–3197. PMLR, 2021.
- [Fatras *et al.*, 2021b] Kilian Fatras, Younes Zine, Szymon Majewski, Rémi Flamary, Rémi Gribonval, and Nicolas Courty. Minibatch optimal transport distances: analysis and applications. *arXiv preprint arXiv:2101.01792*, 2021.
- [Feydy *et al.*, 2019] Jean Feydy, Thibault Séjourné, François-Xavier Vialard, Shun-ichi Amari, Alain Trouvé, and Gabriel Peyré. Interpolating between optimal transport and mmd using sinkhorn divergences. In *The 22nd International Conference on Artificial Intelligence and Statistics*, pages 2681–2690. PMLR, 2019.
- [Folland, 1999] Gerald B Folland. *Real analysis: modern techniques and their applications*, volume 40. John Wiley & Sons, 1999.
- [Gao *et al.*, 2019] Yuan Gao, Yuling Jiao, Yang Wang, Yao Wang, Can Yang, and Shunkang Zhang. Deep generative learning via variational gradient flow. In *ICML*, pages 2093–2101. PMLR, 2019.
- [Gao *et al.*, 2022] Yuan Gao, Jian Huang, Yuling Jiao, Jin Liu, Xiliang Lu, and Zhijian Yang. Deep generative learning via euler particle transport. In *Mathematical and Scientific Machine Learning*, pages 336–368. PMLR, 2022.
- [Genevay *et al.*, 2016] Aude Genevay, Marco Cuturi, Gabriel Peyré, and Francis Bach. Stochastic optimization for large-scale optimal transport. *NeurIPS*, 29, 2016.
- [Genevay *et al.*, 2018] Aude Genevay, Gabriel Peyré, and Marco Cuturi. Learning generative models with sinkhorn divergences. In *International Conference on Artificial Intelligence and Statistics*, pages 1608–1617. PMLR, 2018.
- [Goodfellow *et al.*, 2014] Ian Goodfellow, Jean Pouget-Abadie, Mehdi Mirza, Bing Xu, David Warde-Farley, Sherjil Ozair, Aaron Courville, and Yoshua Bengio. Generative adversarial nets. *NeurIPS*, 27, 2014.
- [Grathwohl *et al.*, 2018] Will Grathwohl, Ricky TQ Chen, Jesse Bettencourt, Ilya Sutskever, and David Duvenaud. Ffjord: Free-form continuous dynamics for scalable reversible generative models. *arXiv preprint arXiv:1810.01367*, 2018.
- [Heng *et al.*, 2022] Alvin Heng, Abdul Fatir Ansari, and Harold Soh. Deep generative wasserstein gradient flows. 2022.
- [Heusel *et al.*, 2017] Martin Heusel, Hubert Ramsauer, Thomas Unterthiner, Bernhard Nessler, and Sepp Hochreiter. Gans trained by a two time-scale update rule converge to a local nash equilibrium. *NeurIPS*, 30, 2017.
- [Ho *et al.*, 2020] Jonathan Ho, Ajay Jain, and Pieter Abbeel. Denoising diffusion probabilistic models. *NeurIPS*, 33:6840–6851, 2020.
- [Hsieh *et al.*, 2021] Ya-Ping Hsieh, Panayotis Mertikopoulos, and Volkan Cevher. The limits of min-max optimization algorithms: Convergence to spurious non-critical sets. In *ICML*, pages 4337–4348. PMLR, 2021.

- [Jordan *et al.*, 1998] Richard Jordan, David Kinderlehrer, and Felix Otto. The variational formulation of the fokker–planck equation. *SIAM journal on mathematical analysis*, 29(1):1–17, 1998.
- [Kalantari, 2007] Iraj Kalantari. *Induction over the Continuum*, pages 145–154. Springer Netherlands, Dordrecht, 2007.
- [Komatsu *et al.*, 2021] Tatsuya Komatsu, Tomoko Matsui, and Junbin Gao. Multi-source domain adaptation with sinkhorn barycenter. In *2021 29th European Signal Processing Conference (EUSIPCO)*, pages 1371–1375. IEEE, 2021.
- [Korotin *et al.*, 2021] Alexander Korotin, Lingxiao Li, Aude Genevay, Justin M Solomon, Alexander Filippov, and Evgeny Burnaev. Do neural optimal transport solvers work? a continuous wasserstein-2 benchmark. *NeurIPS*, 34:14593–14605, 2021.
- [Li *et al.*, 2017] Chun-Liang Li, Wei-Cheng Chang, Yu Cheng, Yiming Yang, and Barnabás Póczos. Mmd gan: Towards deeper understanding of moment matching network. *NeurIPS*, 30, 2017.
- [Lipman *et al.*, 2023] Yaron Lipman, Ricky T. Q. Chen, Heli Ben-Hamu, Maximilian Nickel, and Matthew Le. Flow matching for generative modeling. In *The Eleventh ICLR*, 2023.
- [Liu *et al.*, 2023] Xingchao Liu, Chengyue Gong, and qiang liu. Flow straight and fast: Learning to generate and transfer data with rectified flow. In *The Eleventh ICLR*, 2023.
- [Liutkus *et al.*, 2019] Antoine Liutkus, Umut Simsekli, Szymon Majewski, Alain Durmus, and Fabian-Robert Stöter. Sliced-wasserstein flows: Nonparametric generative modeling via optimal transport and diffusions. In *ICML*, pages 4104–4113. PMLR, 2019.
- [Luise *et al.*, 2019] Giulia Luise, Saverio Salzo, Massimiliano Pontil, and Carlo Ciliberto. Sinkhorn barycenters with free support via frank-wolfe algorithm. *NeurIPS*, 32, 2019.
- [Mnih *et al.*, 2013] Volodymyr Mnih, Koray Kavukcuoglu, David Silver, Alex Graves, Ioannis Antonoglou, Daan Wierstra, and Martin Riedmiller. Playing atari with deep reinforcement learning. *arXiv preprint arXiv:1312.5602*, 2013.
- [Mokrov *et al.*, 2021] Petr Mokrov, Alexander Korotin, Lingxiao Li, Aude Genevay, Justin M Solomon, and Evgeny Burnaev. Large-scale wasserstein gradient flows. *NeurIPS*, 34:15243–15256, 2021.
- [Mroueh and Rigotti, 2020] Youssef Mroueh and Mattia Rigotti. Unbalanced sobolev descent. *NeurIPS*, 33:17034–17043, 2020.
- [Mroueh *et al.*, 2019] Youssef Mroueh, Tom Sercu, and Anant Raj. Sobolev descent. In *The 22nd International Conference on Artificial Intelligence and Statistics*, pages 2976–2985. PMLR, 2019.
- [Pai *et al.*, 2021] Gautam Pai, Jing Ren, Simone Melzi, Peter Wonka, and Maks Ovsjanikov. Fast sinkhorn filters: Using matrix scaling for non-rigid shape correspondence with functional maps. In *Proceedings of the IEEE/CVF Conference on Computer Vision and Pattern Recognition*, pages 384–393, 2021.
- [Patrini *et al.*, 2020] Giorgio Patrini, Rianne Van den Berg, Patrick Forre, Marcello Carioni, Samarth Bhargav, Max Welling, Tim Genewein, and Frank Nielsen. Sinkhorn autoencoders. In *Uncertainty in Artificial Intelligence*, pages 733–743. PMLR, 2020.
- [Peyré *et al.*, 2017] Gabriel Peyré, Marco Cuturi, et al. Computational optimal transport. *Center for Research in Economics and Statistics Working Papers*, (2017-86), 2017.
- [Platen and Bruti-Liberati, 2010] Eckhard Platen and Nicola Bruti-Liberati. *Numerical solution of stochastic differential equations with jumps in finance*, volume 64. Springer Science & Business Media, 2010.
- [Pooladian *et al.*, 2023] Aram-Alexandre Pooladian, Heli Ben-Hamu, Carles Domingo-Enrich, Brandon Amos, Yaron Lipman, and Ricky Chen. Multisample flow matching: Straightening flows with minibatch couplings. *arXiv preprint arXiv:2304.14772*, 2023.
- [Salimans *et al.*, 2016] Tim Salimans, Ian Goodfellow, Wojciech Zaremba, Vicki Cheung, Alec Radford, and Xi Chen. Improved techniques for training gans. *NeurIPS*, 29, 2016.
- [Santambrogio, 2015] Filippo Santambrogio. Optimal transport for applied mathematicians. *Birkhäuser, NY*, 55(58-63):94, 2015.
- [Santambrogio, 2017] Filippo Santambrogio. {Euclidean, metric, and Wasserstein} gradient flows: an overview. *Bulletin of Mathematical Sciences*, 7:87–154, 2017.
- [Shaul *et al.*, 2023] Neta Shaul, Ricky TQ Chen, Maximilian Nickel, Matthew Le, and Yaron Lipman. On kinetic optimal probability paths for generative models. In *ICML*, pages 30883–30907. PMLR, 2023.
- [Shen *et al.*, 2020] Zebang Shen, Zhenfu Wang, Alejandro Ribeiro, and Hamed Hassani. Sinkhorn barycenter via functional gradient descent. *NeurIPS*, 33:986–996, 2020.
- [Silver *et al.*, 2016] David Silver, Aja Huang, Chris J Maddison, Arthur Guez, Laurent Sifre, George Van Den Driessche, Julian Schrittwieser, Ioannis Antonoglou, Veda Panneershelvam, Marc Lanctot, et al. Mastering the game of go with deep neural networks and tree search. *nature*, 529(7587):484–489, 2016.
- [Song and Ermon, 2019] Yang Song and Stefano Ermon. Generative modeling by estimating gradients of the data distribution. *NeurIPS*, 32, 2019.
- [Song *et al.*, 2021] Yang Song, Jascha Sohl-Dickstein, Diederik P Kingma, Abhishek Kumar, Stefano Ermon, and Ben Poole. Score-based generative modeling through stochastic differential equations. In *ICLR*, 2021.
- [Süli and Mayers, 2003] Endre Süli and David F Mayers. *An introduction to numerical analysis*. Cambridge university press, 2003.
- [Tong *et al.*, 2023] Alexander Tong, Nikolay Malkin, Guillaume Huguet, Yanlei Zhang, Jarrid Rector-Brooks, Kilian FATRAS, Guy Wolf, and Yoshua Bengio. Improving and generalizing flow-based generative models with minibatch optimal transport. In *ICML Workshop on New Frontiers in Learning, Control, and Dynamical Systems*, 2023.
- [Villani and others, 2009] Cédric Villani et al. *Optimal transport: old and new*, volume 338. Springer, 2009.
- [Wang *et al.*, 2018] Wei Wang, Yuan Sun, and Saman Halgamuge. Improving mmd-gan training with repulsive loss function. *arXiv preprint arXiv:1812.09916*, 2018.
- [Zhang and Katsoulakis, 2023] Benjamin J Zhang and Markos A Katsoulakis. A mean-field games laboratory for generative modeling. *arXiv preprint arXiv:2304.13534*, 2023.
- [Zhang *et al.*, 2021a] Chao Zhang, Zhijian Li, Hui Qian, and Xin Du. Dpvi: A dynamic-weight particle-based variational inference framework. *arXiv preprint arXiv:2112.00945*, 2021.
- [Zhang *et al.*, 2021b] Yufeng Zhang, Siyu Chen, Zhuoran Yang, Michael Jordan, and Zhaoran Wang. Wasserstein flow meets replicator dynamics: A mean-field analysis of representation learning in actor-critic. *NeurIPS*, 34:15993–16006, 2021.

A Computation of \mathcal{W}_ε -potentials

The \mathcal{W}_ε -potentials is the cornerstone to conduct NSGF. Hence, a key component of our method is to efficiently compute this quantity. [Genevay *et al.*, 2016] provided an efficient method when both μ and ν are discrete measures so that we can calculate \mathcal{W}_ε -potential in terms of samples. In particular, when μ is discrete, f can be simply represented by a finite-dimensional vector since only its values on $\text{supp}(\mu)$ matter.

To more clearly explain the relationship between the calculation of \mathcal{W}_ε -potentials and the composition of our algorithm, we provide the following explanation: In practice, we actually calculate the \mathcal{W}_ε -potentials for the empirical distribution of discrete minibatches and construct Sinkhorn WGF based on this. Therefore, in fact, the μ and ν in the subsequent text refer to $(\tilde{X}_i^t)_{i=1}^n$ and $(\tilde{Y}_i^t)_{i=1}^n$ in the Algorithm 1. We first introduce another property of the entropy-regularized optimal transport problem.

Lemma 2. Define the Sinkhorn mapping: $\mathcal{A} : \mathcal{C}(\mathcal{X}) \times \mathcal{M}_1^+(\mathcal{X}) \rightarrow \mathcal{C}(\mathcal{X})$

$$\mathcal{A}(f, \mu)(y) = -\varepsilon \log \int_{\mathcal{X}} \exp((f(x) - c(x, y))/\varepsilon) d\mu(x). \quad (17)$$

The pair $(f_{\mu, \nu}, g_{\mu, \nu})$ are the \mathcal{W}_ε -potentials of the entropy-regularized optimal transport problem 2 if they satisfy:

$$\begin{aligned} f_{\mu, \nu} &= \mathcal{A}(g_{\mu, \nu}, \nu), \mu - a.e. \quad \text{and} \\ g_{\mu, \nu} &= \mathcal{A}(f_{\mu, \nu}, \mu), \nu - a.e., \end{aligned} \quad (18)$$

or equivalently

$$\begin{aligned} \int_{\mathcal{X}} h(x, y) d\nu(y) &= 1, \mu - a.e. , \\ \int_{\mathcal{X}} h(x, y) d\mu(x) &= 1, \nu - a.e. , \end{aligned} \quad (19)$$

where $h(x, y) := \exp \frac{1}{\gamma} (f(x) + g(x) - c(x, y))$.

To be more precise, by plugging in the optimality condition on $g_{\mu, \nu}$ in 1, the dual problem 2 becomes:

$$\text{OT}_\varepsilon(\mu, \nu) = \max_{f \in \mathcal{C}} \langle f, \mu \rangle + \langle \mathcal{A}(f, \mu), \nu \rangle \quad (20)$$

Viewing the discrete measure μ as a weight vector \mathbf{w}_μ on $\text{supp}(\mu)$, we have:

$$\text{OT}_\varepsilon(\mu, \nu) = \max_{\mathbf{f} \in \mathbb{R}^d} \{ F(\mathbf{f}) := \mathbf{f}^\top \mathbf{w}_\mu + \mathbb{E}_{y \sim \nu} [\mathcal{A}(\mathbf{f}, \mu)(y)] \}, \quad (21)$$

that is, we get a standard concave stochastic optimization problem, where the randomness of the problem comes from ν [Genevay *et al.*, 2016]. Hence, the problem can be solved using stochastic gradient descent (SGD). In our methods, we can treat the computation of \mathcal{W}_ε -potentials as a Blackbox. In practice, we use the efficient implementation of the Sinkhorn algorithm with GPU acceleration from the GeomLoss package [Feydy *et al.*, 2019].

B Theory of Sinkhorn Wasserstein gradient flow

Definition 3. (First variation of Functionals over Probability). Given a functional $\mathcal{F} : \mathcal{P}(\mathcal{X}) \rightarrow \mathbb{R}^+$, we shall perturb

measure μ with a perturbation χ so that $\mu + t\chi$ belongs to $\mathcal{P}(\mathcal{X})$ for small t ($\int d\chi = 0$). We treat $\mathcal{F}(\mu)$, as a functional over probability in its second argument and compute its first variation as follows:

$$\frac{d}{dt} \mathcal{F}(\mu + t\chi) \Big|_{t=0} = \lim_{t \rightarrow 0} \frac{\mathcal{F}(\mu + t\chi) - \mathcal{F}(\mu)}{t} := \int \frac{\delta \mathcal{F}}{\delta \mu}(\mu) d\chi. \quad (22)$$

B.1 Proof of Theorem 1

Proof. According to definition 3, given $\mathcal{F}_\varepsilon(\cdot) = \mathcal{S}_\varepsilon(\cdot, \mu^*)$ and t in a neighborhood of 0, we define $\mu_t = \mu + t\delta\mu$

$$\begin{aligned} \lim_{t \rightarrow 0} \frac{1}{t} (\mathcal{F}_\varepsilon(\mu_t) - \mathcal{F}_\varepsilon(\mu)) &= \underbrace{\lim_{t \rightarrow 0} \frac{1}{t} (\mathcal{W}_\varepsilon(\mu_t, \mu^*) - \mathcal{W}_\varepsilon(\mu, \mu^*))}_{\Delta_t^{\text{first part}}} \\ &\quad - \underbrace{\lim_{t \rightarrow 0} \frac{1}{2t} (\mathcal{W}_\varepsilon(\mu_t, \mu_t) - \mathcal{W}_\varepsilon(\mu, \mu))}_{\Delta_t^{\text{second part}}} \end{aligned}$$

We first analysis $\Delta_t^{\text{first part}} := \lim_{t \rightarrow 0} \frac{1}{t} (\mathcal{W}_\varepsilon(\mu_t, \mu^*) - \mathcal{W}_\varepsilon(\mu, \mu^*))$. First, let us remark that (f, g) is the a suboptimal pair of dual potentials $\mathcal{W}_{\varepsilon, \mu^*}(\mu)$ for short. Recall 3,

$$\mathcal{W}_\varepsilon \geq \langle \mu_t, f \rangle + \langle \mu^*, g \rangle - \varepsilon \left\langle \mu_t \otimes \mu^*, \exp \left(\frac{1}{\varepsilon} (f \oplus g - C) \right) - 1 \right\rangle,$$

and thus, since

$$\mathcal{W}_\varepsilon \geq \langle \mu, f \rangle + \langle \mu^*, g \rangle - \varepsilon \left\langle \mu \otimes \mu^*, \exp \left(\frac{1}{\varepsilon} (f \oplus g - C) \right) - 1 \right\rangle,$$

one has

$$\begin{aligned} \Delta_t^{\text{first part}} &\geq \langle \delta\mu, f \rangle - \varepsilon \left\langle \delta\mu \otimes \mu^*, \exp \left(\frac{1}{\varepsilon} (f \oplus g - C) \right) \right\rangle + o(1) \\ &\geq \langle \delta\mu, f - \varepsilon \rangle + o(1) \end{aligned}$$

Conversely, let us denote by (f_t, g_t) the optimal pair of potentials for $\mathcal{W}_\varepsilon(\mu_t, \mu^*)$ satisfying $g_t(x_o) = 0$ for some arbitrary anchor point $x_o \in \mathcal{X}$. As (f_t, g_t) are suboptimal potentials for $\mathcal{W}_\varepsilon(\mu, \mu^*)$ we get that

$$\mathcal{W}_\varepsilon \geq \langle \mu, f_t \rangle + \langle \mu^*, g_t \rangle - \varepsilon \left\langle \mu_t \otimes \mu^*, \exp \left(\frac{1}{\varepsilon} (f \oplus g - C) \right) - 1 \right\rangle,$$

and thus, since

$$\mathcal{W}_\varepsilon \geq \langle \mu_t, f_t \rangle + \langle \mu^*, g_t \rangle - \varepsilon \left\langle \mu_t \otimes \mu^*, \exp \left(\frac{1}{\varepsilon} (f_t \oplus g - C) \right) - 1 \right\rangle,$$

one has

$$\begin{aligned} \Delta_t^{\text{first part}} &\geq \langle \delta\mu, f_t \rangle - \varepsilon \left\langle \delta\mu \otimes \mu_t^*, \exp \left(\frac{1}{\varepsilon} (f_t \oplus g - C) \right) \right\rangle + o(1) \\ &\geq \langle \delta\mu, f_t - \varepsilon \rangle + o(1) \end{aligned}$$

Now, let us remark that as t goes to 0, $\mu + t\delta\mu \rightharpoonup \mu$. f_t and g_t converge uniformly towards f and g according to Proposition 13 [Feydy *et al.*, 2019]. we get

$$\Delta_t^{\text{first part}} = \langle \delta\mu, f \rangle$$

Similar to analysis

$$\Delta_t^{\text{first part}} := \lim_{t \rightarrow 0} \frac{1}{t} (\mathcal{W}_\varepsilon(\mu_t, \mu^*) - \mathcal{W}_\varepsilon(\mu, \mu^*))$$

we define

$$\Delta_t^{\text{second part}} := \lim_{t \rightarrow 0} \frac{1}{2t} (\mathcal{W}_\varepsilon(\mu_t, \mu_t) - \mathcal{W}_\varepsilon(\mu, \mu))$$

, we have:

$$\Delta_t^{\text{second part}} = \langle \delta\mu, f' \rangle$$

to be more clearly, we denote $f = f_{\mu, \mu^*}$ and $f' = f_{\mu, \mu}$ thus,

$$\lim_{t \rightarrow 0} \frac{1}{t} (\mathcal{F}_\varepsilon(\mu_t) - \mathcal{F}_\varepsilon(\mu)) = \langle \delta\mu, f_{\mu, \mu^*} - f_{\mu, \mu} \rangle.$$

So the first variation of \mathcal{F}_ε is:

$$\frac{\delta \mathcal{F}_\varepsilon}{\delta \mu} = f_{\mu, \mu^*} - f_{\mu, \mu}.$$

□

B.2 Proof of Proposition 2

Following the lines of our proof in Theorem 1, we give the following proof.

Lemma 3. (Fréchet derivative of entropy-regularized Wasserstein distance) Let $\varepsilon > 0$. We shall fix in the following a measure μ^* and let $(f_{\mu, \mu^*}, g_{\mu, \mu^*})$ be the \mathcal{W}_ε potentials of $\mathcal{W}_\varepsilon(\mu, \mu^*)$ according to lemma 1. Consider the infinitesimal transport $T(x) = x + \lambda\phi$. We have the Fréchet derivative under this particular perturbation:

$$\begin{aligned} \frac{d}{d\lambda} \mathcal{W}_\varepsilon(T_\# \mu, \mu^*)|_{\lambda=0} &= \lim_{\lambda \rightarrow 0} \frac{\mathcal{W}_\varepsilon(T_\# \mu, \mu^*) - \mathcal{W}_\varepsilon(\mu, \mu^*)}{\lambda} \\ &= \int_{\mathcal{X}} \nabla f_{\mu, \mu^*}(\mathbf{x}) \phi(\mathbf{x}) d\mu(\mathbf{x}). \end{aligned} \quad (23)$$

Proof. let $f = f_{\mu, \mu^*}$ and $g = g_{\mu, \mu^*}$ be the \mathcal{W}_ε -potentials 1 to $\mathcal{W}_\varepsilon(\mu, \mu^*)$ for short. By 3 and the optimality of (f, g) , we have follows:

$$\mathcal{W}_\varepsilon(\mu, \mu^*) = \langle f, \mu \rangle + \langle g, \mu^* \rangle.$$

However, (f, g) are not necessarily the optimal dual variables for $\mathcal{W}_\varepsilon(T_\# \mu, \mu^*)$, recall the lemma 2:

$\mathcal{W}_\varepsilon(T_\# \mu, \mu^*) \geq \langle f, T_\# \mu \rangle + \langle g, \mu^* \rangle - \varepsilon \langle h - 1, T_\# \mu \otimes \mu^* \rangle$, where $\int_{\mathcal{X}} h(\mathbf{x}, \mathbf{y}) d\mu^*(\mathbf{y}) = 1$ and hence $\langle h - 1, T_\# \mu \otimes \mu^* \rangle = 0$. Thus:

$$\mathcal{W}_\varepsilon(T_\# \mu, \mu^*) - \mathcal{W}_\varepsilon(\mu, \mu^*) \geq \langle f, T_\# \mu - \mu \rangle.$$

Use the change-of-variables formula of the push-forward measure to obtain:

$$\begin{aligned} \frac{1}{\lambda} \langle f, T_\# \mu - \mu \rangle &= \frac{1}{\lambda} \int_{\mathcal{X}} ((f \circ T)(\mathbf{x}) - f(\mathbf{x})) d\mu(\mathbf{x}) \\ &= \int_{\mathcal{X}} \nabla f(x + \lambda'\phi(x)) \phi(x) d\mu(\mathbf{x}), \end{aligned}$$

where $\lambda' \in [0, \lambda]$ is from the mean value theorem. Here we assume ∇f is Lipschitz continuous follow Proposition 12 in

[Feydy *et al.*, 2019] and Lemma A.4 form [Shen *et al.*, 2020]. We have:

$$\lim_{\lambda \rightarrow 0} \frac{1}{\lambda} \langle f, T_\# \mu - \mu \rangle = \int_{\mathcal{X}} \nabla f(\mathbf{x}) \phi(\mathbf{x}) d\mu(\mathbf{x}).$$

Hence:

$$\lim_{\lambda \rightarrow 0} \frac{1}{\lambda} (\mathcal{W}_\varepsilon(T_\# \mu, \mu^*) - \mathcal{W}_\varepsilon(\mu, \mu^*)) \geq \int_{\mathcal{X}} \nabla f(\mathbf{x}) \phi(\mathbf{x}) d\mu(\mathbf{x}).$$

Similarly, let f' and g' be the \mathcal{W}_ε potentials to $\mathcal{W}_\varepsilon(T_\# \mu, \mu^*)$, we have:

$$\mathcal{W}_\varepsilon(\mu, \mu^*) \geq \langle f', \mu \rangle + \langle g, \mu^* \rangle - \varepsilon \langle h - 1, \mu \otimes \mu^* \rangle,$$

where $\int_{\mathcal{X}} h(\mathbf{x}, \mathbf{y}) d\mu^*(\mathbf{y}) = 1$ and hence $\langle h - 1, \mu \otimes \mu^* \rangle = 0$. Thus:

$$\mathcal{W}_\varepsilon(T_\# \mu, \mu^*) - \mathcal{W}_\varepsilon(\mu, \mu^*) \leq \langle f', T_\# \mu - \mu \rangle.$$

Same as above, use the change-of-variables formula and the mean value theorem:

$$\frac{1}{\lambda} \langle f', T_\# \mu - \mu^* \rangle = \int_{\mathcal{X}} \nabla f'(x + \lambda'\phi(x)) \phi(x) d\mu(\mathbf{x}),$$

Thus:

$$\begin{aligned} \lim_{\lambda \rightarrow 0} \frac{1}{\lambda} (\mathcal{W}_\varepsilon(T_\# \mu, \mu^*) - \mathcal{W}_\varepsilon(\mu, \mu^*)) &\leq \\ \int_{\mathcal{X}} \lim_{\lambda \rightarrow 0} \nabla f'(x + \lambda'\phi(x)) \phi(x) d\mu(\mathbf{x}). \end{aligned}$$

Assume that $\nabla f'$ is Lipschitz continuous and $f' \rightarrow f$ as $\lambda \rightarrow 0$. Consequently we have $\lim_{\lambda \rightarrow 0} \nabla f'(x + \lambda'\phi(x))$ and hence:

$$\lim_{\lambda \rightarrow 0} \frac{1}{\lambda} (\mathcal{W}_\varepsilon(T_\# \mu, \mu^*) - \mathcal{W}_\varepsilon(\mu, \mu^*)) = \int_{\mathcal{X}} \nabla f(\mathbf{x}) \phi(\mathbf{x}) d\mu(\mathbf{x}).$$

According to lemma 3, we have:

$$\begin{aligned} \left. \frac{d}{d\lambda} \mathcal{F}_\varepsilon(T_\# \mu) \right|_{\lambda=0} &= \int_{\mathcal{X}} \nabla f_{\mu, \mu^*}(\mathbf{x}) \phi(\mathbf{x}) d\mu(\mathbf{x}) \\ &\quad - \frac{1}{2} \cdot \int_{\mathcal{X}} 2 \nabla f_{\mu, \mu}(\mathbf{x}) \phi(\mathbf{x}) d\mu(\mathbf{x}) \\ &= \int_{\mathcal{X}} \nabla f_{\mu, \mu^*}(\mathbf{x}) \phi(\mathbf{x}) d\mu - \int_{\mathcal{X}} \nabla f_{\mu, \mu}(\mathbf{x}) \phi(\mathbf{x}) d\mu. \end{aligned}$$

□

B.3 Proof of theorem 2

Proof. First, we define $\Psi(\mu) = \int h d\mu$ where $h : \mathbb{R}^d \rightarrow \mathbb{R}$ is an arbitrary bounded and continuous function and $\frac{\delta \Psi(\mu)}{\delta \mu}(\mathbf{x})$ denotes the first variation of functional Ψ at μ satisfying:

$$\int \frac{\delta \Psi(\mu)}{\delta \mu}(\mathbf{x}) \xi(\mathbf{x}) dx = \lim_{\epsilon \rightarrow 0} \frac{\Psi(\mu + \epsilon \xi) - \Psi(\mu)}{\epsilon}$$

for all signed measure $\int \xi(\mathbf{x}) dx = 0$. We also have the following:

$$\frac{\delta \Psi(\mu)}{\delta \mu}(\cdot) = \frac{\delta \int h d\mu}{\delta \mu}(\cdot) = h(\cdot)$$

Assume μ_t is a flow satisfies the following:

$$\partial_t \Psi[\mu_t] = (\mathcal{L}\Psi)[\mu_t],$$

where,

$$\mathcal{L}\Psi[\mu_t] = - \int \langle \nabla \frac{\delta \mathcal{F}_\varepsilon(\mu_t)}{\delta \mu}(\mathbf{x}), \nabla_{\mathbf{x}} \frac{\delta \Psi(\mu_t)}{\delta \mu}(\mathbf{x}) \rangle \mu_t(\mathbf{x}) d\mathbf{x} \quad (24)$$

Notably, μ_t is a solution of equation 2.

Next, let $\tilde{\mu}_t^M$ be the distribution produced by the equation 14 at time t . Under mild assumption of $\tilde{\mu}_0^M \rightharpoonup \mu_0$, we want to show that the mean-field limit of $\tilde{\mu}_t^M$ as $M \rightarrow \infty$ is μ_t by showing that $\lim_{M \rightarrow \infty} \Psi(\tilde{\mu}_t^M) = \Psi(\mu_t)$ [Folland, 1999].

For the measure valued flow $\tilde{\mu}_t^M$ equation 14, the infinitesimal generator of Ψ w.r.t. $\tilde{\mu}_t^M$ is defined as follows:

$$(\mathcal{L}\Psi)[\tilde{\mu}_t^M] := \lim_{\epsilon \rightarrow 0^+} \frac{\Psi(\tilde{\mu}_{t+\epsilon}^M) - \Psi(\tilde{\mu}_t^M)}{\epsilon},$$

According to the definition of first variation, it can be calculated that

$$\begin{aligned} (\mathcal{L}\Psi)[\tilde{\mu}_t^M] &= \lim_{\epsilon \rightarrow 0^+} \frac{\Psi[\sum_{i=1}^M \frac{1}{M} \delta_{\mathbf{x}_{t+\epsilon}^i}] - \Psi(\sum_{i=1}^M \frac{1}{M} \delta_{\mathbf{x}_t^i})}{\epsilon} \\ &= \int \frac{\delta \Psi(\tilde{\mu}_t^M)}{\delta \mu}(\mathbf{x}) \sum_{i=1}^M \frac{1}{M} \partial_t \rho(\mathbf{x}_t^i) d\mathbf{x} \end{aligned}$$

Then we adopt the *Induction over the Continuum* to prove $\lim_{n \rightarrow \infty} \Psi(\tilde{\mu}_t^M) = \Psi(\mu_t)$ for all $t > 0$. Here $t \in \mathbb{R}^+$ satisfy the requirement of well ordering and the existence of a greatest lower bound for non-empty subsets, so *Induction over the Continuum* is reasonable [Kalantari, 2007].

1. As for $t = 0$, our assumption of $\tilde{\mu}_0^M \rightharpoonup \mu_0$ suffice.
2. For the case of $t = t^*$, we first hypothesis that for $t < t^*$, $\tilde{\mu}_t^M \rightharpoonup \mu_t$ as $M \rightarrow \infty$. Then for $t < t^*$ we have:

$$\begin{aligned} &\lim_{M \rightarrow \infty} (\mathcal{L}\Psi)[\tilde{\mu}_t^M] \\ &= \lim_{M \rightarrow \infty} \int \frac{\delta \Psi(\tilde{\mu}_t^M)}{\delta \mu}(\mathbf{x}) \sum_{i=1}^M \frac{1}{M} \partial_t \rho(\mathbf{x}_t^i) d\mathbf{x} \\ &= - \lim_{M \rightarrow \infty} \int \langle \nabla \frac{\delta \mathcal{F}_\varepsilon(\mu_t)}{\delta \mu}(\mathbf{x}), \nabla_{\mathbf{x}} \frac{\delta \Psi(\tilde{\mu}_t^M)}{\delta \mu}(\mathbf{x}) \rangle \tilde{\mu}_t^M(\mathbf{x}) d\mathbf{x} \\ &= - \int \langle \nabla \frac{\delta \mathcal{F}_\varepsilon(\mu_t)}{\delta \mu}(\mathbf{x}), \nabla_{\mathbf{x}} \frac{\delta \Psi(\mu_t)}{\delta \mu}(\mathbf{x}) \rangle \mu_t(\mathbf{x}) d\mathbf{x}. \end{aligned}$$

Because $\lim_{M \rightarrow \infty} \Psi(\tilde{\mu}_0^M) = \Psi(\mu_0)$ at $t = 0$ and $\lim_{M \rightarrow \infty} (\partial_t \Psi)[\tilde{\mu}_t^M] = (\partial_t \Psi)[\mu_t]$ for all $t < t^*$, we have $\lim_{M \rightarrow \infty} \Psi(\tilde{\mu}_{t^*}^M) = \Psi(\mu_{t^*})$.

Combining (1) and (2), we can reach to the conclusion that $\lim_{M \rightarrow \infty} \Psi(\tilde{\mu}_t^M) = \Psi(\mu_t)$ for all t . which indicates that $\tilde{\mu}_t^M \rightharpoonup \mu_t$ if $\tilde{\mu}_0^M \rightharpoonup \mu_0$. Since μ_t solves the partial differential equation 10, we conclude that the path of equation 14 starting from $\tilde{\mu}_0^M$ weakly converges to a solution of the partial differential equation equation 10 starting from μ_0 as $M \rightarrow \infty$. \square

B.4 Descending property

Proposition 3. Consider the Sinkhorn gradient flow 10, the differentiation of $\mathcal{F}_\varepsilon(\mu_t)$ with respect to the time t satisfies:

$$\frac{d\mathcal{F}_\varepsilon(\mu_t)}{dt} = - \int \left\| \nabla \left(\frac{\delta \mathcal{F}_\varepsilon(\mu_t)}{\delta \mu_t} \right) \right\|^2 d\mu_t \leq 0 \quad (25)$$

Proof. By substituting $\Psi(\cdot) = \mathcal{F}_\varepsilon(\cdot)$ in equation 24, we directly reach to the above equality. \square

C Minibatch Optimal Transport

For large datasets, the computation and storage of the optimal transport plan can be challenging due to OT's cubic time and quadratic memory complexities relative to the number of samples [Cuturi, 2013; Genevay *et al.*, 2016; Peyré *et al.*, 2017]. The minibatch approximation offers a viable solution for enhancing calculation efficiency. Theoretical analysis of using the minibatch approximation for transportation plans is provided by [Fatras *et al.*, 2019; Fatras *et al.*, 2021b]. Although minibatch OT introduces some errors compared to the exact OT solution, its efficiency in computing approximate OT is clear, and it has seen successful applications in domains like domain adaptation [Damodaran *et al.*, 2018; Fatras *et al.*, 2021a] and generative modeling [Genevay *et al.*, 2018].

More recently, [Pooladian *et al.*, 2023; Tong *et al.*, 2023] introduced OT-CFM and empirically demonstrated that using minibatch approximation of optimal transport in flow matching methods [Liu *et al.*, 2023; Lipman *et al.*, 2023] can straighten the flow's trajectory and yield more consistent samples. OT-CFM specifically focuses on minibatch initial and target samples, continuing to use random linear interpolation paths. In contrast, NSGF leverages minibatch \mathcal{W}_ε -potentials to construct Sinkhorn gradient flows in minibatches. Our method also involves performing velocity field matching on the flow's discretized form, marking a separate and innovative direction in the field.

D NSGF++

We introduce a two-phase NSGF++ algorithm that initially employs the Sinkhorn gradient flow for rapid approximation to the image manifold, followed by sample refinement using a straightforward straight flow. The NSGF++ model comprises three key components:

- An NSGF model trained for $T \leq 5$ time steps.
- A phase-transition time predictor, denoted as $t_\phi : \mathcal{X} \rightarrow [0, 1]$, which facilitates the transition from NSGF to NSF.
- A Neural Straight Flow (NSF) model, trained through velocity field matching on a linear interpolation straight flow $X_t \sim (1-t)P_0 + tP_1, t \in [0, 1]$.

the detailed algorithm is outlined in 3.

In the inference process of NSGF++, we initially apply the NSGF with fewer than 5 NFE, starting from $X_0 \sim P_0$, to obtain an intermediate output \hat{X}_T . This output is then processed using the time predictor t_ϕ . The final output is achieved by refining this intermediate result with the NSF model, starting

Algorithm 3: NSGF++ Training

```

Input : number of time steps  $T$ , batch size  $n$ , gradient flow step size  $\eta > 0$ , empirical or samplable distribution  $\mu_0$  and  $\mu^*$ , neural network parameters  $\theta$ , optimizer step size  $\gamma > 0$ 

/* NSGF model */  

/* Build trajectory pool */  

while Building do  

    /* Sample batches of size  $n$  i.i.d. from the datasets */  

     $\tilde{X}_i^0 \sim \mu_0, \tilde{Y}_i \sim \mu^*, i = 1, 2, \dots, n.$   

    for  $t = 0, 1, \dots, T$  do  

        calculate  $f_{\tilde{\mu}_t, \tilde{\mu}_t}(\tilde{X}_i^t), f_{\tilde{\mu}_t, \tilde{\mu}^*}(\tilde{X}_i^t)$ .  

         $\hat{v}_{\mu_t}^{\mathcal{F}_e}(\tilde{X}_i^t) = \nabla f_{\tilde{\mu}_t, \tilde{\mu}_t}(\tilde{X}_i^t) - \nabla f_{\tilde{\mu}_t, \tilde{\mu}^*}(\tilde{X}_i^t)$ .  

         $\tilde{X}_i^{t+1} = \tilde{X}_i^t + \eta \hat{v}_t^{\mathcal{F}_e}(\tilde{X}_i^t).$   

        store all  $(\tilde{X}_i^t, \hat{v}_t^{\mathcal{F}_e}(\tilde{X}_i^t))$  pair into the pool,  $i = 1, 2, \dots, n.$   

/* velocity field matching */  

while Not convergence do  

    from trajectory pool sample pair  $(\tilde{X}_i^t, \hat{v}_t^{\mathcal{F}_e}(\tilde{X}_i^t))$ .  

     $\mathcal{L}(\theta) = \|v^\theta(\tilde{X}_i^t, t) - \hat{v}_{\mu_t}^{\mathcal{F}_e}(\tilde{X}_i^t)\|^2,$   

     $\theta \leftarrow \theta - \gamma \nabla_\theta \mathcal{L}(\theta).$   

/* phase transition time predictor */  

while Training do  

     $\tilde{X}_i^0 \sim \mu_0, \tilde{Y}_i \sim \mu^*, i = 1, 2, \dots, n.$   

     $t \sim \mathcal{U}(0, 1).$   

     $X_t = t \tilde{Y}_i + (1-t) \tilde{X}_i^0$   

     $\mathcal{L}(\phi) = E_{t \in \mathcal{U}(0,1), X_t \sim P_t} \|t - t_\phi(X_t)\|^2.$   

     $\phi \leftarrow \phi - \gamma' \nabla_\phi \mathcal{L}(\phi).$   

/* NSF model */  

while Training do  

     $\tilde{X}_i^0 \sim \mu_0, \tilde{Y}_i \sim \mu^*, i = 1, 2, \dots, n.$   

     $t \sim \mathcal{U}(0, 1).$   

     $X_t = t \tilde{Y}_i + (1-t) \tilde{X}_i^0.$   

     $\mathcal{L}_{\text{NSF}}(\delta) \leftarrow \|u_\delta(t, X_t) - (\tilde{Y}_i - \tilde{X}_i^0)\|^2.$   

     $\delta \leftarrow \delta - \gamma'' \nabla_\delta \mathcal{L}_{\text{NSF}}(\delta).$   

Output:  $v_\theta$  parameterize the time-varying velocity field of NSGF,  $t_\phi$  parameterize the phase transition time predictor,  $u_\delta$  parameterize the NSF model

```

from the state $t_\phi(\tilde{X}_t)$. The detailed algorithm is outlined in 4.

E Experiments

E.1 2D simulated data

For the 2D experiments, we closely follow [Tong *et al.*, 2023] and the released code at <https://github.com/atong01/conditional-flow-matching> (code released under MIT license), and use the same synthetic datasets and the 2-Wasserstein distance between the test set and samples simulated using NSGF as the evaluation metric. We use 1024 samples in the test set since we find the We use a simple MLP with 3 hidden layers and 256 hidden units to parameterize the velocity matching networks. We use batch size 256 and 10/100 steps with a uniform schedule at sampling time. For both Nerual gradient-flow-

based models and Nerual ODE-based Models, we train for 20000 steps in total. Note that FM cannot be used for the 8gaussians-moons task since it requires a Gaussian source, but we still conducted experiments with the algorithm and found competitive experimental results. We believe that this is because FM is essentially very close to 1-RF in its algorithmic design, and that the Gaussian source condition can be meaningfully relaxed in practice, as confirmed in [Tong *et al.*, 2023]. The experiments are run using one 3090 GPU and take approximately less than 60 minutes (for both training and testing).

For the neural gradient-flow-based models, we solely implemented the EPT without the outer loop, as the outer loop can be likened to a GAN-like distillation approach [Goodfellow *et al.*, 2014]. Notably, the original EPT [Gao *et al.*, 2022] recommends iterating for 20,000 rounds with an exceedingly

Algorithm 4: NSGF++ Inference

Input : number of NSGF time steps $T \leq 5$, NSGF++ inference step size η , NSGF velocity field v^θ , phase transition time predictor t_ϕ , NSF inference step size ω , NSF model u^δ , prior samples $\tilde{X}_i^0 \sim \tilde{\mu}_0$, $ODEsolver(X, model, starttime, endtime, steps)$

```

/* NSGF phase
for t = 0, 1, ..., T do
     $\tilde{X}_i^{t+1} = \tilde{X}_i^t + \eta v^\theta(\tilde{X}_i^t, t)$ , i = 1, 2, ..., n.
/* phase transition time predict
 $\hat{t} = t_\phi(\tilde{X}_i^T)$ .
/* NSF refine phase
 $\hat{T} = (1 - \hat{t})/\omega$ .
 $\tilde{X} = ODEsolver(\tilde{X}_i^T, u^\delta, \hat{t}, 1, \hat{T})$ .
Output:  $\tilde{X}$  as the results.
```

small step size; however, to ensure a fair comparison, we employed the same number of steps as the other methods while adapting the step size accordingly. It's worth mentioning that for the JKO-Flow, we used the recommended parameter setting of 10 steps, as suggested in [Fan *et al.*, 2022], but we also provide results for 100 steps for comparative purposes. All the results for Neural Gradient flow-based models were trained and sampled following the standard procedures outlined in their respective papers.

E.2 Image benchmark data

For the MNIST/CIFAR-10 experiments, we summarize the setup of our NSGF++ model here, where the exact parameter choices can be seen in the source code. For the calculation of \mathcal{W}_ϵ -potentials, we use the GeomLoss package [Feydy *et al.*, 2019] with blur = 0.5, 1.0 or 2.0, scaling = 0.80, 0.85 or 0.95 depends on learning rate of Sinkhorn gradient flow. We find using an incremental lr scheme will improve training performance. More detailed experiments we will leave for future work. We used the Adam optimizer with $\beta_1 = 0.9, \beta_2 = 0.999$ and no weight decay. Here we list different part of our NSGF++ model separately. First, we use the UNet architecture from [Dhariwal and Nichol, 2021]. For MNIST, we use channels = 32, depth = 1, channels multiple = [1, 2, 2], heads = 1, attention resolution = 16, dropout = 0.0. For CIFAR-10, we use channels = 128, depth = 2, channels multiple = [1, 2, 2, 2], heads = 4, heads channels = 64, attention resolution = 16, dropout = 0.0. We use the same UNet architecture in our neural straight flow model.

For the phase transition time predictor, we employed an efficiently designed convolutional neural network (CNN) capable of achieving satisfactory results while optimizing training time. The CNN used in our study consists of a structured architecture featuring four convolutional layers with filter depths of 32, 64, 128, and 256. Each layer uses a 3x3 kernel, a stride of 1, and padding of 1, coupled with ReLU activation and 2x2 average pooling for effective feature downsampling. The network culminates in a fully connected layer that transforms the flattened features into a single value, further

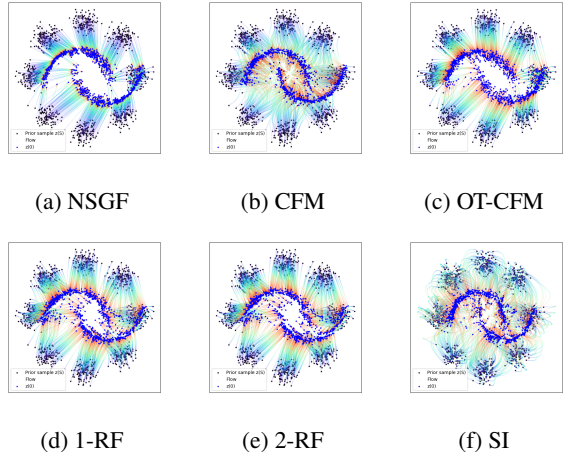


Figure 6: Visualization results for 2D generated paths. We show different methods that drive the particle from the prior distribution (black) to the target distribution (blue). The color change of the flow shows the different number of steps (from blue to red means from 0 to T). We can see NSGF using fewer steps than OT-CFM

refined through a sigmoid activation function for regression tasks targeting time value outputs. This architecture is tailored for processing image inputs to predict continuous time values within a specific range. The training parameters are as follows: Batch size: 128 Learning rate: 10^{-4} . For sampling, a 5-step Euler integration is applied in the NSGF phase on MNIST and CIFAR-10 datasets. Training the phase transition time predictor is efficient and methodically streamlined. Utilizing a well-structured CNN as its backbone, the model reaches peak performance in merely 20 minutes, covering 40,000 iterations. This training efficiency is a significant advantage, especially for applications that demand rapid model adaptation.

For the MNIST/CIFAR-10 experiments, a considerable amount of storage space is required when establishing the trajectory pool during the first phase of the algorithm. For MNIST dataset, setting the batch size to 256 and saving 1500 batches 5-step minibatch Sinkhorn gradient flow trajectories requires less than 20GB of storage space and with CIFAR-10, setting the batch size to 128 and saving 2500 batches 5-step minibatch Sinkhorn gradient flow trajectories requires about 45GB of storage space. In situations where storage space is limited, we suggest dynamically adding and removing trajectories in the trajectory pool to meet the training requirements. Identifying a more effective trade-off between training time and storage space utilization is a direction for future improvement.

E.3 Supplementary experimental results

2D simulated data

In our supplementary materials, we present additional results from 2D simulated data to demonstrate the efficiency of the NSGF++ model in Figure 6 and Figure 7. These results indicate that NSGF++ achieves competitive performance with a more direct path and fewer steps compared to other neural Wasserstein gradient flow and flow-matching methods, highlighting its effectiveness and computational efficiency.

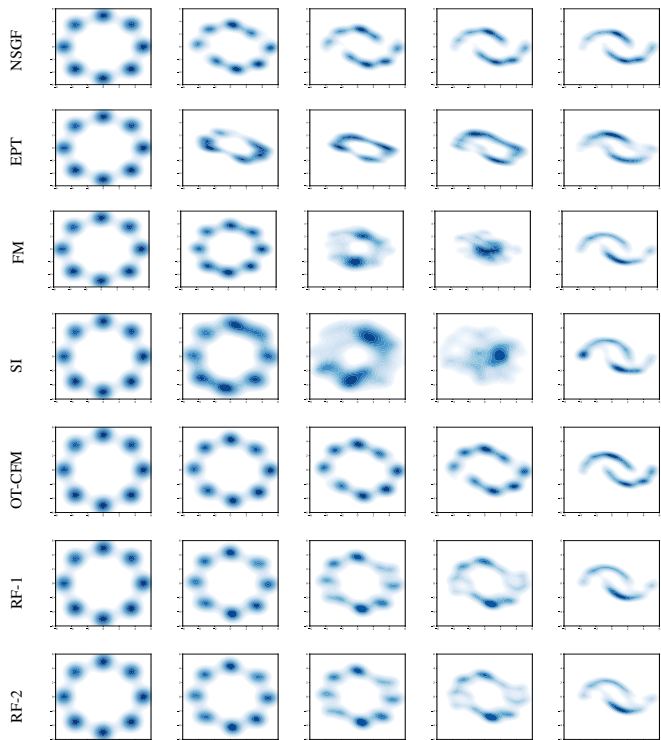


Figure 7: 2-Wasserstein Distance of the generated process utilizing neural ODE-based diffusion models and NSGF. The FM/SI methods reduce noise roughly linearly, while NSGF quickly recovers the target structure and progressively optimizes the details in subsequent steps.

MNIST

In our study, we include results from the MNIST dataset to showcase the efficiency of the NSGF++ model. As detailed in Table 3, NSGF++ achieves competitive Fréchet Inception Distances (FIDs) while utilizing only 60% of the Number of Function Evaluations (NFEs) typically required. This underscores the model’s effectiveness in balancing performance with computational efficiency. To evaluate our results, we use the Fréchet inception distance (FID) between 10K generated samples and the test dataset. Here, a smaller FID value indicates a higher similarity between generated and test samples.

CIFAR-10

In our work, we present further results of the NSGF++ model on the CIFAR-10 dataset, illustrated in Figures 9 and 11. These experimental findings demonstrate that NSGF++ attains competitive performance in generation tasks, highlighting its efficacy.

Algorithm	MNIST	
	FID(\downarrow)	NFE(\downarrow)
NSGF++(ours)	3.8	60
SWG[2019]	225.1	500
SIG[2020]	4.5	/
FM [2023]	3.4	100
OT-CFM [2023]	3.3	100
RF [2023]	3.1	100
Training set	2.27	/

Table 3: Comparison of NSGF++ and other methods over MNIST, The last row states statistics of the FID scores between 10k training examples and 10k test examples

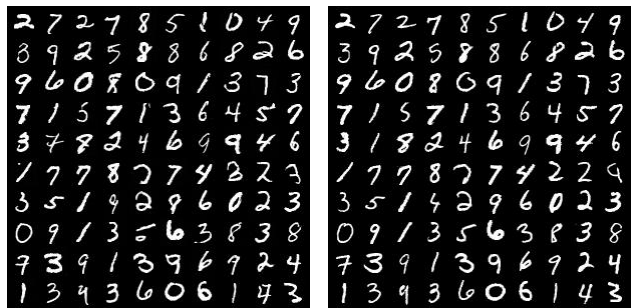


Figure 8: Uncurated samples on MNIST and L_2 -nearest neighbors from the training set (top: Samples, bottom: real) We observe that they are significantly different. Hence, our method generates really new samples and is not just reproducing the samples from the training set

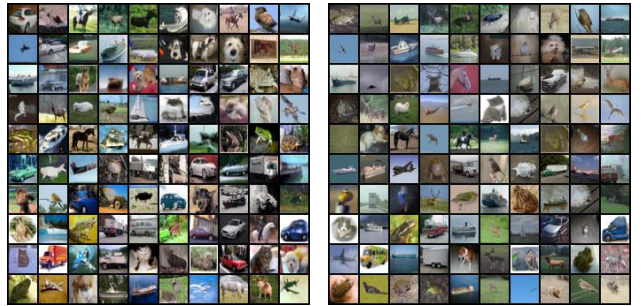


Figure 9: Uncurated samples on CIFAR-10 and L_2 -nearest neighbors from the training set (top: Samples, bottom: real)

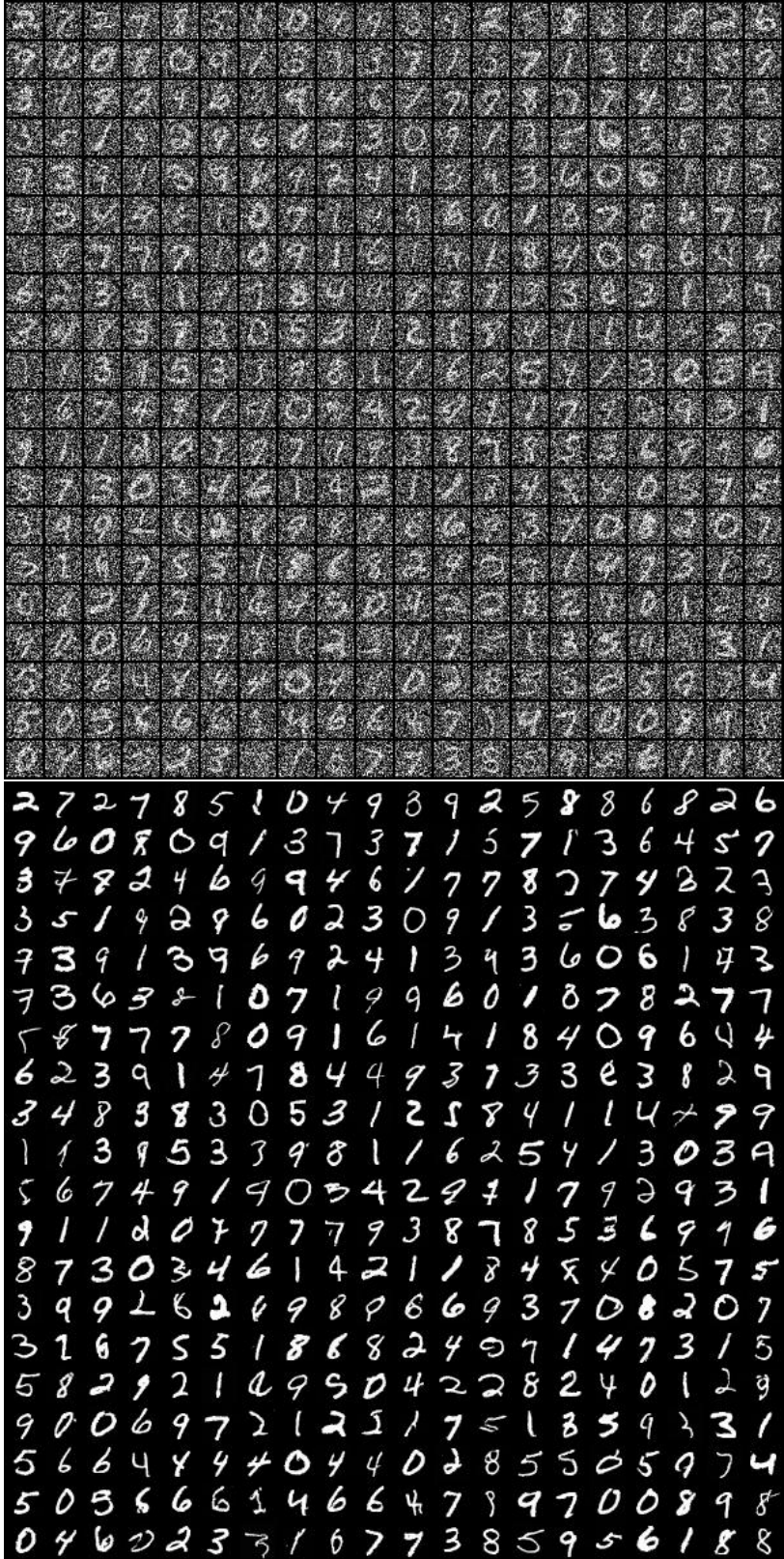


Figure 10: The extensive inference result of our NSGF++ model on MNIST. The first row shows the result after 5 NSGF steps and the second row shows the final results

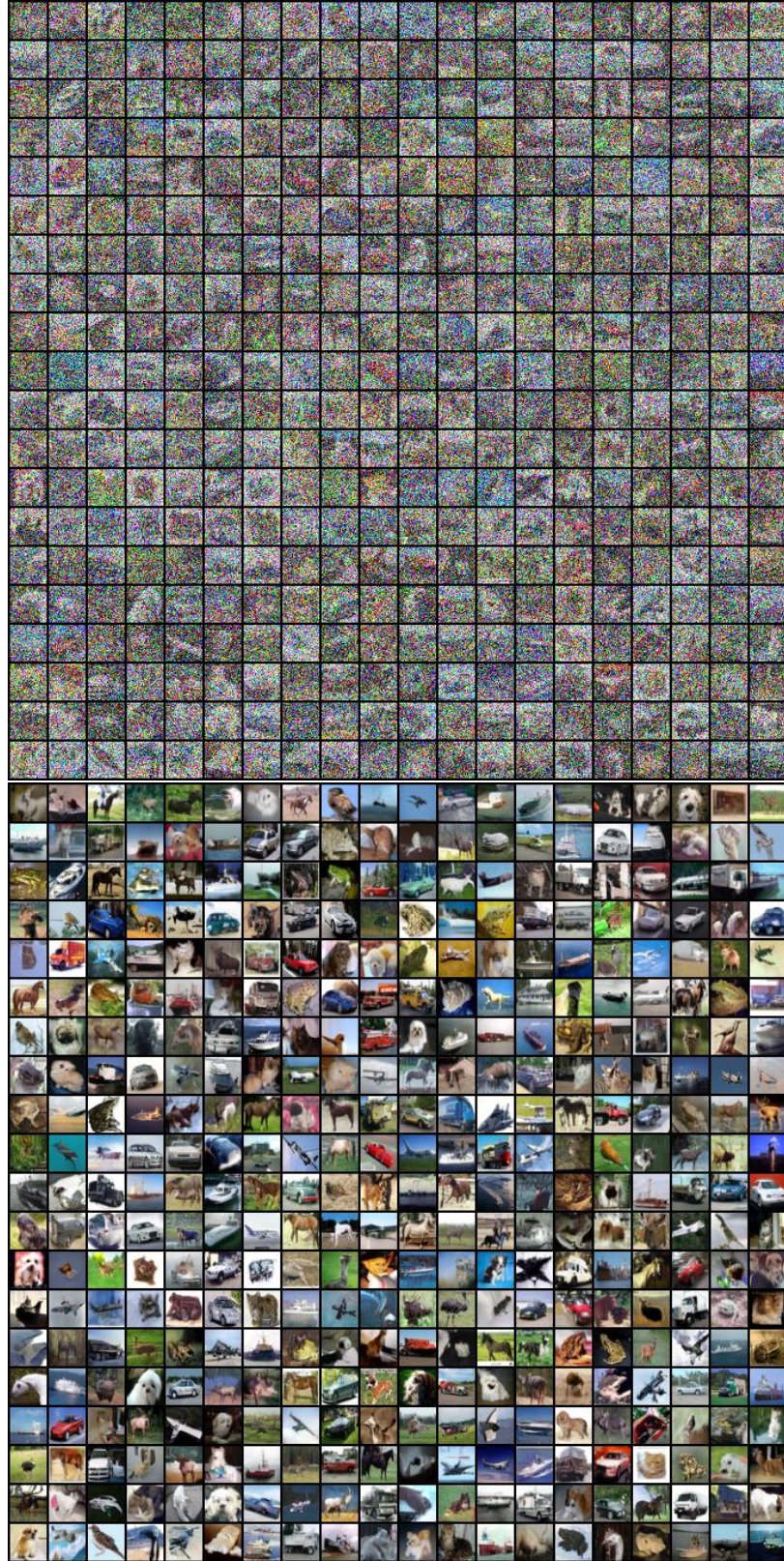


Figure 11: The extensive inference result of our NSGF++ model on CIFAR-10. The first row shows the result after 5 NSGF steps and the second row shows the final results